Acta Crystallographica Section A
Foundations of Crystallography
ISSN 0108-7673

Received 3 April 2013
Accepted 23 May 2013

Influence of Bragg diffraction on perfect crystal neutron phase shifters and the exact solution of the two-beam case in the dynamical diffraction theory

Hartmut Lemmel

Vienna University of Technology, Atominstitut, 1020 Wien, Austria, and Institut Laue–Langevin, 38000 Grenoble, France. Correspondence e-mail: hartmut@lemmel.at

The phase shift of neutrons passing through a sample is usually determined by the sample's index of refraction based on the coherent neutron scattering length. If the sample has a perfect crystal structure there are, however, additional phase effects due to Bragg diffraction. While Bragg peaks in the diffracted direction are very sharp on the angular scale, the phase of the transmitted beam is influenced on a much wider angular range in the order of degrees around the Bragg condition. The magnitude of this effect is in the order of 10^{-4} of the refractive phase and clearly visible in interferometry measurements on a perfect silicon sample. In order to calculate the effect, the exact solution is derived for the two-beam case of the dynamical diffraction theory for arbitrary Bragg-plane orientation and arbitrary deviations from the Bragg condition. Even far off any Bragg condition, a residual phase correction remains which is identified as a local field correction.

1. Introduction

The coherent neutron scattering length b_c is an important parameter for various kinds of scattering measurements and can be determined only experimentally for most nuclides. b_c enters in the index of refraction n or the quantum mechanical phase shift χ of neutrons in matter as

$$n = 1 - \lambda^2 N b_c/(2\pi), \quad \chi = -\lambda N b_c D, \tag{1}$$

where λ is the neutron wavelength, N the number density and D the thickness of the sample slab. Neutron interferometry (Rauch & Werner, 2000) is one of the most sensitive methods for b_c determination, especially if high-purity samples with $D \gtrsim 1$ cm are available. These criteria are ideally met by perfect crystals and the most precise b_c value determined so far is that of silicon, obtained by the interferometric measurement of a perfect crystal silicon sample (Ioffe *et al.*, 1998). The accuracy was in the order of 10^{-4}. During our work to improve this method (Lemmel & Wagh, 2010) we have noticed that the perfect crystal structure creates additional phase effects due to Bragg diffraction. Even if the beam angle is several degrees off any Bragg condition, the phase shift of the sample might be changed by about 10^{-4}. In the work of Ioffe *et al.* (1998) two slightly different experimental results are given which have been measured independently with different setups and wavelengths. The discrepancy is larger than the individual errors and it seems likely to us that it has been caused by Bragg diffraction.

Crystalline samples are described by the theory of dynamical diffraction. The standard dynamical theory was developed in the 1920s to describe Bragg diffraction of X-rays, reviewed in Batterman & Cole (1964) and Authier (2006). Later on, the theory was adapted to neutrons (*cf. e.g.* Bauspiess *et al.*, 1976; Bonse & Graeff, 1977; Petrascheck, 1976) and extended to special cases of grazing incident and exit angles, reviewed in Authier (1998, 2006). In all these works emphasis was given to diffraction angles in the vicinity of the Bragg condition where the diffracted-beam intensity does not vanish. As a consequence, approximations for small Bragg-angle deviations were used and the phase effects that occur for larger Bragg-angle deviations in transmission were obscured and underestimated for a long time. The first detailed description was our exact calculation of the symmetrical Laue case (Lemmel, 2007). Now we present the calculation for the general case of arbitrary Bragg-plane orientation and show how to use it to correct for diffraction effects in scattering-length measurements.

In §2 we examine the transmitted phase theoretically and find a very general approximation for large Bragg-angle deviations which is valid for any Bragg-plane orientation. The approximation is derived from the exact symmetric Bragg and Laue formulas and then numerically checked against the general exact solution of the two-beam case given in the Appendix. In §3 we apply the theory to our particular experimental setup, taking the beam divergence and wavelength distribution into account. We determine all possible Bragg diffractions in the crystalline sample, apply the phase corrections and compare the results with our alignment scans where we rotated and tilted the sample into various Bragg conditions. Results and conclusions are discussed in §§4 and 5.

2. Plane-wave solutions of the two-beam case

We assume a non-absorbing sample with perfect crystal structure. The two-beam case of the dynamical diffraction theory describes Bragg diffraction on a single set of reflecting planes. The two beams refer to the forward and diffracted directions in the crystal. Other sets of Bragg planes as well as higher-order reflections are neglected. Then the solution of the Schrödinger equation inside the crystal leads to two coupled equations (*cf. e.g.* Bonse & Graeff, 1977; Rauch & Werner, 2000):

$$\left(\frac{K^2}{k^2}-1+\frac{V_0}{E}\right)u=-\frac{V_{-H}}{E}u_H, \tag{2}$$

$$\left(\frac{K_H^2}{k^2}-1+\frac{V_0}{E}\right)u_H=-\frac{V_H}{E}u. \tag{3}$$

k, K and H are the absolute values of $\mathbf{k}$, $\mathbf{K}$ and $\mathbf{H}$, respectively, where $\mathbf{k}$ denotes the incident wavevector outside the crystal, $\mathbf{K}$ the forward wavevector inside the crystal and $\mathbf{K}_H=\mathbf{K}+\mathbf{H}$ the wavevector in the diffracted direction. E denotes the neutron energy $E=\hbar^2k^2/(2m)$ with the neutron mass m. V_0 denotes the neutron optical potential $V_0=2\pi\hbar^2Nb_c/m$ with the coherent scattering length b_c and the atom number density N of the sample material. V_H denotes the diffracting potential and depends on H and the crystal structure. For a silicon crystal and the Miller indices h, j, l we get

$$V_H=\begin{cases}V_0 & \text{if } h,j,l \text{ are all even and}\\ & h+j+l \text{ divisible by 4,}\\ V_0(1+i)/2 & \text{if } h,j,l \text{ are all odd.}\end{cases} \tag{4}$$

We consider a crystal slab with parallel front and back surface and thickness D (Fig. 1). The surfaces are perpendicular to the z axis. The wavevectors as well as the reciprocal-lattice vector $\mathbf{H}$ lie in the x/z plane. With the continuity condition $K_x=k_x$ and the abbreviations $v_{0,H}=V_{0,H}/E$, $\overline{H}=H/k$, $\overline{K}=K/k$, $\overline{K}_{x,z}=K_{x,z}/k$, $\overline{k}_{x,z}=k_{x,z}/k$, $\overline{\kappa}_z=(\overline{k}_z^2-v_0)^{1/2}$ we obtain from equations (2) and (3)

$$|v_H|^2=\left(\overline{K}_z^2-\overline{\kappa}_z^2\right)\left(\overline{K}_z^2+2\overline{H}_z\overline{K}_z+\overline{H}^2+2\overline{H}_x\overline{k}_x-\overline{\kappa}_z^2\right), \tag{5}$$

which is a fourth-order (quartic) equation in $\overline{K}_z$. The wavevectors $\mathbf{K}$ and $\mathbf{K}_H$ and their amplitudes u and u_H are to be determined.

The transmitted component has the amplitude t and the same wavevector as the incident wave $\mathbf{k}_T=\mathbf{k}$. We denote the diffracted wavevector exiting on the front surface (Bragg case) by $\mathbf{k}_\mathrm{B}$ with the amplitude b and the diffracted wavevector exiting on the back surface (Laue case) by $\mathbf{k}_\mathrm{L}$ with the amplitude l. Inside the crystal the wavevector may be altered only by the reciprocal-lattice vector $\mathbf{H}$. The k_x component is conserved on both surfaces and the k_z components of the exiting beams follow from energy conservation. Thus the vectors outside the crystal are given by

$$\mathbf{k}=\begin{pmatrix}k_x\\ k_z\end{pmatrix},\quad \mathbf{k}_\mathrm{L}=\begin{pmatrix}k_x+H_x\\ k_{\mathrm{L}z}\end{pmatrix},\quad \mathbf{k}_\mathrm{B}=\begin{pmatrix}k_x+H_x\\ -k_{\mathrm{L}z}\end{pmatrix}, \tag{6}$$

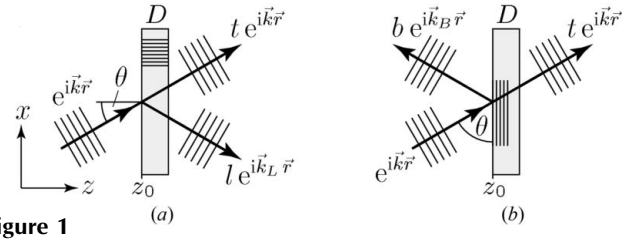

Figure 1
Incident and exit wavevectors for the symmetric Laue (*a*) and Bragg (*b*) case.

$$k_{\mathrm{L}z}=[k^2-(k_x+H_x)^2]^{1/2}. \tag{7}$$

First we solve the symmetric Bragg and Laue cases for large violations of the Bragg condition. We make approximations for small crystal potentials and we neglect surface reflections. Then we show that the results are also valid for the asymmetric cases by comparing them numerically with the general exact solution of the two-beam case given in the Appendix.

2.1. Symmetric Laue case

The symmetric Laue case is described in detail in Lemmel (2007). Let us summarize and improve the results. In the symmetric Laue case $H_x=-H$ and $H_z=0$ and the solution of equation (5) reads

$$\overline{K}_{z1,2,(3,4)}=(\pm)\{\overline{\kappa}_z^2+|v_H|[-\eta_\mathrm{L}\pm(1+\eta_\mathrm{L}^2)^{1/2}]\}^{1/2} \tag{8}$$

with

$$\eta_\mathrm{L}=-\frac{H^2}{|v_H|k^2}\left(\frac{k_x}{H}-\frac{1}{2}\right). \tag{9}$$

η_L is a dimensionless parameter specifying the deviation from the Bragg condition. We neglect the solutions $\overline{K}_{z3,4}=-\{\ldots\}^{1/2}$ which refer to the components reflected on the back surface, moving in a negative z direction. With the ansatz

$$\psi_\mathrm{I}=\exp(i\mathbf{kr}),\quad z\le z_0, \tag{10}$$

$$\psi_\mathrm{II}=u_1\exp(i\mathbf{K}_1\mathbf{r})+u_{H1}\exp[i(\mathbf{K}_1+\mathbf{H})\mathbf{r}]+u_2\exp(i\mathbf{K}_2\mathbf{r})+u_{H2}\exp[i(\mathbf{K}_2+\mathbf{H})\mathbf{r}],\quad z_0\le z\le z_0+D, \tag{11}$$

$$\psi_\mathrm{III}=t_\mathrm{L}\exp(i\mathbf{kr})+l_\mathrm{L}\exp(i\mathbf{k}_\mathrm{L}\mathbf{r}),\quad z_0+D\le z \tag{12}$$

and with the continuity conditions $\psi_\mathrm{I}=\psi_\mathrm{II}$ at $z=z_0$ and $\psi_\mathrm{II}=\psi_\mathrm{III}$ at $z=z_0+D$ we obtain (Lemmel, 2007)

$$t_\mathrm{L}=\exp(-ik_zD)\left[\frac{\exp(iK_{z1}D)+\exp(iK_{z2}D)}{2}+\frac{\eta_\mathrm{L}}{(1+\eta_\mathrm{L}^2)^{1/2}}\times\frac{\exp(iK_{z1}D)-\exp(iK_{z2}D)}{2}\right], \tag{13}$$

$$l_\mathrm{L}=\exp(-ik_zD)\exp[i(k_z-k_{Lz})(D+z_0)]\left(\frac{V_H}{V_{-H}}\right)^{1/2}\times\frac{-1}{(1+\eta_\mathrm{L}^2)^{1/2}}\frac{\exp(iK_{z1}D)-\exp(iK_{z2}D)}{2}. \tag{14}$$

In order to separate dynamical diffraction effects from the normal phase shifter behaviour we factorize the transmission factor into a refractive and a diffractive part,

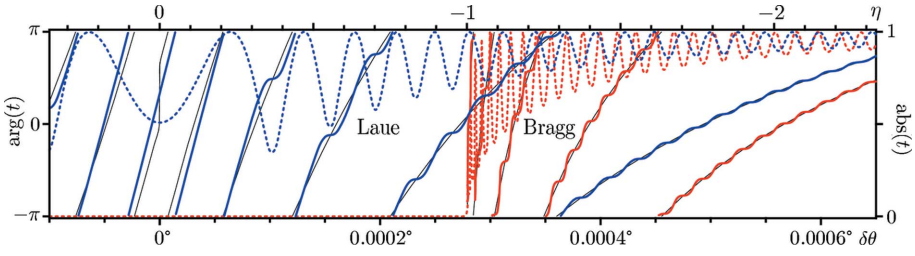

Figure 2
Argument value (solid lines, left axis) and absolute value (dotted lines, right axis) of the transmission factor t for the symmetrical Bragg case (red) and Laue case (blue) as a function of deviation parameters $\delta\theta$ (lower scale) or η (upper scale) closely around the Bragg condition. In the Bragg case no intensity is transmitted around $\delta\theta = 0$ (Darwin plateau). The *Pendellösung* oscillations in the absolute value come together with little step-like features in the argument value. The thin black lines show the phase averaged over the *Pendellösung* oscillations [*cf.* text and equations (45), (46)]. The plot has been calculated for a 220 silicon crystal of thickness 0.5 mm and wavelength $\lambda = 2.7155$ Å.

$$t_{\rm L} = t_{\rm ref}\, t_{\rm difL}, \tag{15}$$

$$t_{\rm ref} = \exp(i\chi_{\rm ref}), \tag{16}$$

$$\chi_{\rm ref} = D(\kappa_z - k_z), \tag{17}$$

$$\kappa_z = (k_z^2 - k^2 v_0)^{1/2}. \tag{18}$$

Then equations (13) and (14) become, with a first-order expansion of $(K_{z1,2} - \kappa_z)$ by v_H which is in the order of 10^{-6},

$$t_{\rm L} = t_{\rm ref}\exp(-iA_{\rm L}\eta_{\rm L})\left\{\cos\left[A_{\rm L}(1+\eta_{\rm L}^2)^{1/2}\right] + \frac{i\eta_{\rm L}}{(1+\eta_{\rm L}^2)^{1/2}} \times \sin\left[A_{\rm L}(1+\eta_{\rm L}^2)^{1/2}\right]\right\}, \tag{19}$$

$$l_{\rm L} = t_{\rm ref}\exp(-iA_{\rm L}\eta_{\rm L})\frac{\exp[i(k_z - k_{Lz})(D+z_0)]}{i(1+\eta_{\rm L}^2)^{1/2}} \times \sin\left[A_{\rm L}(1+\eta_{\rm L}^2)^{1/2}\right]\left(\frac{V_H}{V_{-H}}\right)^{1/2}, \tag{20}$$

$$A_{\rm L} = \frac{Dk^2|v_H|}{2\kappa_z} = \frac{Dm|V_H|}{\hbar^2\kappa_z}. \tag{21}$$

Note that the $A_{\rm L}$ defined here contains the refracted vector component κ_z inside the crystal whereas the A_H of Lemmel (2007) or other papers contains the incident component k_z. This way the result is more elegant and even more accurate than our previous result (Lemmel, 2007). In particular the transition $t_{\rm L} \to t_{\rm ref}$ for large $|\eta_{\rm L}|$ is more obvious: if $(1+\eta_{\rm L}^2)^{1/2} \to |\eta_{\rm L}|$ the term in braces in equation (19) cancels with the exponential term and only $t_{\rm ref}$ is left.

The Laue result is plotted in Fig. 2 (blue curves).

2.2. Symmetric Bragg case

In the symmetric Bragg case $H_x = 0$ and $H_z = -H$ and the solution of equation (5) reads

$$K_{z1,2,(3,4)} = \frac{H}{2} \pm \frac{|v_H|k^2}{H}[(\eta_{\rm B}^{(\mp)})^2 - 1]^{1/2}, \tag{22}$$

$$\eta_{\rm B}^{\mp} = \frac{H^2}{|v_H|k^2}\left[\frac{1}{2} \mp \frac{\kappa_z}{H}\left(\frac{v_H^2 k^4}{H^2\kappa_z^2} + 1\right)^{1/2}\right]. \tag{23}$$

Again we neglect the solutions $K_{z3,4} = \ldots(\eta_{\rm B}^{+})^2\ldots$ which refer to the components reflected on the inside of either surface. In addition, we neglect the v_H^2 term in the square root of $\eta_{\rm B}$ as v_H is in the order of 10^{-6}.

$$K_{z1,2} = \frac{H}{2} \pm \frac{|v_H|k^2}{H}(\eta_{\rm B}^2 - 1)^{1/2}, \tag{24}$$

$$\eta_{\rm B} = -\frac{H^2}{|v_H|k^2}\left(\frac{\kappa_z}{H} - \frac{1}{2}\right). \tag{25}$$

In the ansatz we distinguish between forward- and backward-moving wave components denoted by f and b indices, respectively,

$$\psi_{\rm If} = \exp(i\mathbf{kr}), \quad \psi_{\rm Ib} = b_{\rm B}\exp(i\mathbf{k}_{\rm B}\mathbf{r}), \quad z \le z_0, \tag{26}$$

$$\psi_{\rm IIf} = u_1\exp(i\mathbf{K}_1\mathbf{r}) + u_2\exp(i\mathbf{K}_2\mathbf{r}),$$
$$\psi_{\rm IIb} = u_{H1}\exp[i(\mathbf{K}_1+\mathbf{H})\mathbf{r}] + u_{H2}\exp[i(\mathbf{K}_2+\mathbf{H})\mathbf{r}], \quad z_0 \le z \le z_0 + D, \tag{27}$$

$$\psi_{\rm IIIf} = t_{\rm B}\exp(i\mathbf{kr}), \quad \psi_{\rm IIIb} = 0, \quad z_0 + D \le z. \tag{28}$$

The continuity conditions read $\psi_{\rm If,b} = \psi_{\rm IIf,b}$ at $z = z_0$ and $\psi_{\rm IIf,b} = \psi_{\rm IIIf,b}$ at $z = z_0 + D$, and we obtain

$$t_{\rm B} = t_{\rm ref}\frac{\exp(iA_{\rm B}\eta_{\rm B})}{\cos\left[A_{\rm B}(\eta_{\rm B}^2-1)^{1/2}\right] + [i\eta_{\rm B}/(\eta_{\rm B}^2-1)^{1/2}]\sin\left[A_{\rm B}(\eta_{\rm B}^2-1)^{1/2}\right]}, \tag{29}$$

$$b_{\rm B} = \frac{(V_H/V_{-H})^{1/2}}{-\eta_{\rm B} + i(\eta_{\rm B}^2-1)^{1/2}\cot\left[A_{\rm B}(\eta_{\rm B}^2-1)^{1/2}\right]}, \tag{30}$$

$$A_{\rm B} = \frac{Dk^2|v_H|}{H}. \tag{31}$$

The transmission factor $t_{\rm B}$ converges to $t_{\rm ref}$ for large $|\eta_{\rm B}|$ as the exponential cancels with the numerator if $(\eta_{\rm B}^2-1)^{1/2} \to |\eta_{\rm B}|$.

The Bragg result is plotted in Fig. 2 (red curves). Fig. 3 illustrates the total and the refractive phase in a larger angular range around the Bragg condition. Different Bragg-plane orientations are compared, the asymmetric cases are calculated in the Appendix.

2.3. Deviation parameters

The dimensionless parameters $\eta_{\rm L}$ and $\eta_{\rm B}$ specify the deviation from the Bragg condition. Their definitions [equations (9) and (25), respectively] were motivated by the simplification of the symmetric case formulas. Nevertheless, we can combine them into a single definition as in the Laue case $k_x = \kappa_x = |\boldsymbol{\kappa}\mathbf{H}|/H$ and in the Bragg case $\kappa_z = |\boldsymbol{\kappa}\mathbf{H}|/H$,

$$\eta = -\frac{H^2}{|v_H|k^2}\left(\frac{\boldsymbol{\kappa}\mathbf{H}}{H^2} - \frac{1}{2}\right). \tag{32}$$

This simple generalization to arbitrary Bragg-plane orientation is useful for our further calculations. However, it should not be used to calculate the Darwin width for asymmetric cases, which would then turn out to be narrower than ±1.

In Figs. 2 and 3 we show both the η and $\delta\theta$ scale. By convention a positive $\delta\theta$, *i.e.* an increase of the angle between beam and lattice planes, corresponds to a negative η,

$$\eta \simeq -\frac{\delta\theta \sin(2\theta_B)}{|v_H|} \quad \text{for } |\delta\theta = \theta - \theta_B| \lesssim 1^\circ. \tag{33}$$

This relation between η and $\delta\theta$ does not include any refraction correction. Usually θ_B is defined by Bragg's law, $k \sin\theta_B = H/2$, relating the outside vector $\mathbf{k}$ to the inside reciprocal-lattice vector $\mathbf{H}$. Then the relation between η and $\delta\theta$ becomes more complex when refraction on the surface is taken into account. As a consequence, the Darwin plateau of the Bragg case ($-1 < \eta < 1$) is not centred around the Bragg angle θ_B. Only in the symmetric Laue case $\delta\theta = 0$ corresponds to $\eta = 0$. Here we try to separate the effects of refraction and diffraction and to compare Bragg and Laue cases. We therefore apply Bragg's law on the refracted wavevector $\boldsymbol{\kappa}$ inside the crystal $\kappa \sin\Theta_B = H/2$ with $\kappa = k(1 - v_0)^{1/2}$. The inside Bragg angle Θ_B is then converted to the outside Bragg angle θ_B by the law of refraction. We equate the tangential components of the inner and outer vectors, $k_x = k\cos(\beta + \theta_B) = \kappa_x = \kappa\cos(\beta + \Theta_B)$, with β denoting the angle between Bragg planes and surface (*cf.* Fig. 3),

$$\cos(\theta_B + \beta) = (1 - v_0)^{1/2} \cos(\Theta_B + \beta), \tag{34}$$

$$\theta_B = -\beta + \arccos\left[(1 - v_0)^{1/2} \cos(\beta + \Theta_B)\right], \tag{35}$$

$$\Theta_B = \arcsin \frac{H}{2k(1 - v_0)^{1/2}}. \tag{36}$$

With this definition of θ_B, equation (33) is valid for all Bragg-plane orientations and both the Laue and the Bragg curves are centred around $\delta\theta = 0$ as shown in Figs. 2 and 3.

We express η by a newly defined parameter $\delta\kappa$ which we will use later on to integrate over the $\mathbf{k}$ distribution of the beam,

$$\eta = -\frac{H^2}{k^2|v_H|}\,\delta\kappa, \tag{37}$$

$$\delta\kappa = \frac{|\boldsymbol{\kappa}\mathbf{H}|}{H^2} - \frac{1}{2}. \tag{38}$$

$\delta\kappa$ can be understood in the following way. The Bragg condition is exactly fulfilled if the projection of the refracted wavevector into the $\mathbf{H}$ direction equals $H/2$. $\delta\kappa$ is the deviation of this projection from the ideal value divided by H to make it dimensionless. The value range of $\delta\kappa$ is given by

$$-\frac{1}{2} \le \delta\kappa \le \frac{\kappa}{H} - \frac{1}{2}. \tag{39}$$

The lower limit is ensured by the modulus in equation (38) and is due to the fact that a sign change of $\boldsymbol{\kappa}\mathbf{H}$ just corresponds to a wave falling from the other side onto the Bragg planes. At the limit $\boldsymbol{\kappa}$ and $\mathbf{H}$ are perpendicular. The upper limit is determined by the general vector inequality $|\boldsymbol{\kappa}\mathbf{H}| \le \kappa H$. In this limit $\boldsymbol{\kappa}$ and $\mathbf{H}$ are collinear.

2.4. Diffractive phase

Fig. 2 shows the phase arg(t) and the modulus abs(t) of a transmitted plane wave close to the Bragg condition for the symmetric Bragg and Laue cases. The modulus (dotted line) shows the well known *Pendellösung* oscillations and vanishes in the Bragg case in the central region (Darwin plateau). The argument value also shows *Pendellösung* features in the form of step-like shapes. These features have already been described for the symmetric Laue case (Lemmel, 2007) and have been verified experimentally (Springer *et al.*, 2010; Springer, 2009) using a highly sophisticated setup. The sample crystal had the same structure and orientation as the interferometer crystal (nondispersive configuration) and a second sample in the other interferometer path compensated for defocusing and for the steep phase slope. In a usual setup, however, the sample crystal has different crystal structure and/or orientation than the interferometer crystal (dispersive configuration). Then a broad range on the η or $\delta\kappa$ scale is excited, much wider than the Darwin width, and the transmission factor has to be averaged over this distribution. In the near range around the Bragg condition the phase slope is very steep and thus the phase spreads over several orders of 2π within the beam divergence. Then the interference contrast vanishes, meaning that the near range is not accessible experimentally. In this paper we therefore focus on the far range and apply a number of approximations to simplify the results for this range.

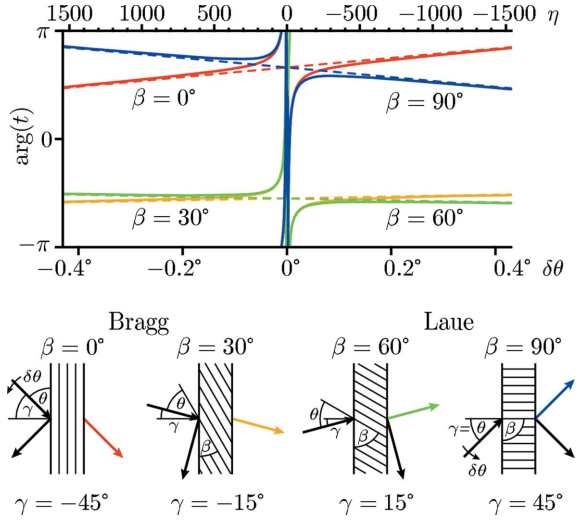

Figure 3
Argument value of the transmission factor as a function of misset angle $\delta\theta$ for different Bragg-plane orientations β. For large $|\delta\theta|$ the argument values approach the refractive phases χ_{ref} shown by the dashed lines. The plot has been calculated for a 220 silicon crystal of 1 mm thickness. The wavelength $\lambda = 2.7155$ Å has been chosen such that the symmetrical Bragg ($\beta = 0^\circ$) and Laue ($\beta = 90^\circ$) cases have incident angles of the same magnitude ($\gamma = \mp 45^\circ$). Thus the Bragg and Laue cases can be directly compared having the same χ_{ref} at $\delta\theta = 0$. Note that χ_{ref} is in the order of $-12.7 \times 2\pi$ and that all phases are plotted modulo 2π. The asymmetric Bragg and Laue cases of $\beta = 30^\circ$ and $\beta = 60^\circ$, respectively, have an incident angle of $\gamma = \mp 15^\circ$ and therefore a smaller phase shift magnitude, $\chi_{ref} = -9.3 \times 2\pi$.

We define the diffractive phase χ_{dif} as the deviation of the total phase from the refractive phase,

$$\chi_{dif} = \chi - \chi_{ref} = \arg(t/t_{ref}). \tag{40}$$

In a previous paper (Springer *et al.*, 2010) we referred to it as the 'Laue phase' since it was measured in Laue geometry. However, it appears equally in Bragg geometry so the name 'diffractive phase' seems more appropriate.

Approximation 1. We average the transmission factors t_L [equation (19)] and t_B [equation (29)] over the *Pendellösung* oscillations as they cannot be resolved anyway with a broad η distribution. t_L oscillates as a function of A_L with the two frequencies $\eta_1 = \eta$ and $\eta_2 = (1+\eta^2)^{1/2}$. The beating between these frequencies creates the *Pendellösung* oscillations. We average t_L around some A_0 over one beating period given by $\Delta A_L = 2\pi/(\eta_1 + \eta_2)$. In the Bragg case we average the expression $1/t_B$ with similar considerations. The results are (with A_0 replaced by $A_{B,L}$ after integration)

$$\langle t_L \rangle = \frac{1}{\Delta A_L} \int_{A_0-\Delta A_L/2}^{A_0+\Delta A_L/2} t_L \, \mathrm{d}A_L \tag{41}$$

$$= t_{\rm ref} \frac{|\eta|}{(1+\eta^2)^{1/2}} \frac{|\eta| + (1+\eta^2)^{1/2}}{-|\eta| + (1+\eta^2)^{1/2}} \times \mathrm{sinc}\big\{2\pi\eta\big[-|\eta| + (1+\eta^2)^{1/2}\big]\big\} \times \exp\big\{iA_L\big[-\eta + \mathrm{sign}\,(\eta)(1+\eta^2)^{1/2}\big]\big\}, \tag{42}$$

$$\langle t_B \rangle = \left(\frac{1}{\Delta A_B} \int_{A_0-\Delta A_B/2}^{A_0+\Delta A_B/2} \frac{1}{t_B} \, \mathrm{d}A_B \right)^{-1} \tag{43}$$

$$= t_{\rm ref} \frac{(\eta^2-1)^{1/2}}{-|\eta|\big[|\eta| + (\eta^2-1)^{1/2}\big]^2} / \mathrm{sinc}\big\{2\pi\eta\big[|\eta| - (\eta^2-1)^{1/2}\big]\big\} \times \exp\big\{-iA_B\big[-\eta + \mathrm{sign}(\eta)(\eta^2-1)^{1/2}\big]\big\}. \tag{44}$$

We can directly read out the resulting diffractive phase:

$$\langle \chi_{\rm difL} \rangle = \arg \frac{\langle t_L \rangle}{t_{\rm ref}} = A_L\big[-\eta + \mathrm{sign}(\eta)(\eta^2+1)^{1/2}\big], \tag{45}$$

$$\langle \chi_{\rm difB} \rangle = \arg \frac{\langle t_B \rangle}{t_{\rm ref}} = A_B\big[\eta - \mathrm{sign}(\eta)(\eta^2-1)^{1/2}\big]. \tag{46}$$

These functions are shown by the thin lines in Fig. 2.

Approximation 2. We make a first-order series expansion of $\langle \chi_{\rm difL,B} \rangle$ by $1/\eta$ to simplify the result for large $|\eta|$,

$$\langle \chi_{\rm difL,B} \rangle \overset{|\eta|\gg 1}{\longrightarrow} \frac{A_{L,B}}{2\eta}. \tag{47}$$

A similar expression for the X-ray case can be found in Authier (2006), §5.5.6, where it has been derived by geometrical considerations on the dispersion surfaces.

So far we have described the symmetric cases. The solution for the asymmetric cases is presented in the Appendix, where the general two-beam case is solved without further approximations, even taking surface reflection into account. Since the general result is quite bulky we want to discuss here only the resulting plots and thus compare it numerically with the symmetric cases. Fig. 4 shows the diffractive phase over the whole possible range of $\delta\kappa$ [*cf.* equation (39)]. The positive and negative $\delta\kappa$ branches are shown in separate plots because of the logarithmic scale. The far-range approximation $\langle \chi_{\rm difL} \rangle$ [equation (47)] derived for the symmetric Laue case is plotted by the black line. The coloured curves show the exact solution for different Bragg-plane orientations. They separate for small $|\delta\kappa|$ but converge to the black line in the far range. The symmetric Laue solution $\arg(t_L)$ [equation (19)] is not distinguishable from the exact Laue solution (blue line). The symmetric Bragg solution $\arg(t_B)$ [equation (29)] differs from the exact solution in the very far range, shown by the thin red line. We conclude that the symmetric Laue formula of the diffractive phase serves as an excellent far-range approximation for all Bragg-plane orientations and denote it further on by $\langle \chi_{\rm dif} \rangle \equiv \langle \chi_{\rm difL} \rangle$.

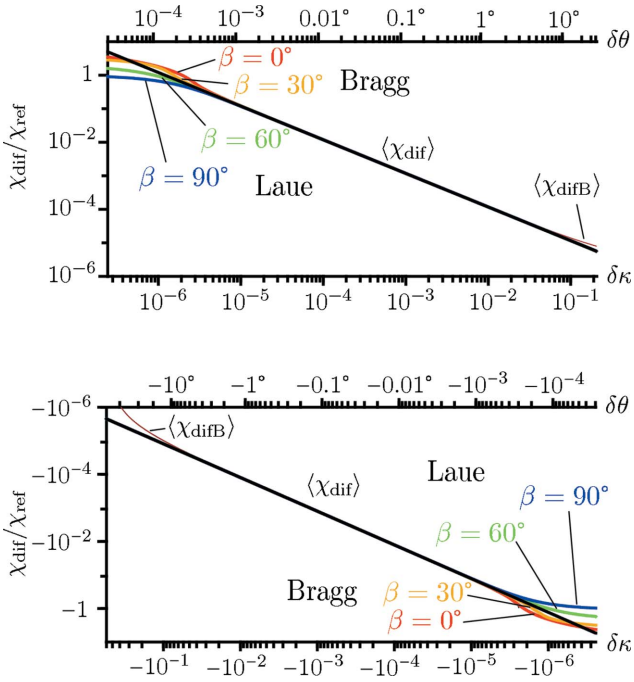

Figure 4
Relative diffractive phase $\chi_{\rm dif}/\chi_{\rm ref}$ as a function of deviation parameter $\delta\kappa$ (lower scale) or Bragg-angle deviation $\delta\theta$ (upper scale) for different Bragg-plane orientations β. The two figures show the positive and negative branch of $\delta\kappa$, respectively. In the far range ($|\delta\theta| \gtrsim 0.001°$) the expression is independent of β and inversely proportional to $\delta\kappa$ (black line), see text. The numerical parameters are the same as in Fig. 3.

Remark on Fig. 4. When calculating the quotient $\chi_{\rm dif}/\chi_{\rm ref} = (\chi - \chi_{\rm ref})/\chi_{\rm ref}$ one needs to know the 2π order of the phases. This is no problem for $\chi_{\rm ref}$ given directly by equation (17) but $\chi = \arg(t)$ is defined only modulo 2π. Accordingly, the plot of $\arg(t)$ in Fig. 2 shows several 2π jumps. In Fig. 4 we start the evaluation of χ at some $|\delta\kappa|$ large enough so that $\chi \simeq \chi_{\rm ref}$ or $\chi_{\rm dif} \simeq 0$. When approaching $\delta\kappa = 0$ we correct for each 2π jump introduced by the arg function and thus obtain a continuous curve of χ. We do this for the positive and negative side of $\delta\kappa$ and thereby accumulate all 2π jumps at $\delta\kappa = 0$. This is convenient for our far-range calculations but be aware that the complex function t is continuous also at $\delta\kappa = 0$. All jumps, wherever they are put, are multiples of 2π and have no physical meaning.

We can write the total phase shift as $\chi = \chi_{\rm ref}(1 + \langle\chi_{\rm rel}\rangle)$ by defining the relative diffractive phase:

$$\langle\chi_{\rm rel}\rangle = \frac{\langle\chi_{\rm dif}\rangle}{\chi_{\rm ref}} = \frac{A_{\rm L}}{2\eta\chi_{\rm ref}} = \frac{k^2|v_H|}{4\eta\kappa_z(\kappa_z - k_z)}. \quad (48)$$

The sample thickness D contained in $A_{\rm L}$ and $\chi_{\rm ref}$ cancels, and with κ_z [equation (18)] and a first-order expansion by v_0 we obtain

$$\langle\chi_{\rm rel}\rangle \simeq -\frac{|v_H|}{v_0 2\eta} = \frac{B}{\delta\kappa}, \qquad B = \frac{|V_H|^2 m}{V_0 \hbar^2 H^2}. \quad (49)$$

B contains only crystal parameters and does not depend on the beam.

Approximation 3. We set the modulus of t to unity. The intensity dip of t close to the Bragg condition reduces the intensity of a divergent beam in dispersive geometry only by a few per mille and the phase in this region is smeared out anyway.

Approximation 4. We describe the $\delta\kappa$ distribution (*i.e.* beam divergence) by a Lorentzian in order to get a solvable integral for the convolution,

$$g(\delta\kappa) = \frac{1}{\pi\sigma_\kappa\left[1 + (\delta\kappa/\sigma_\kappa)^2\right]}. \quad (50)$$

The intensity of a single plane-wave component in the O beam of the interferometer reads for a non-absorbing sample

$$I(\delta\kappa) = 1 + \cos(\chi_{\rm dif} + \chi_{\rm ref} - \varphi) \quad (51)$$

$$= 1 + \cos\left[\left(\frac{B}{\delta\kappa} + 1\right)\chi_{\rm ref} - \varphi\right], \quad (52)$$

where φ denotes the phase contribution of the auxiliary phase flag. Averaged over the $\delta\kappa$ distribution we get (with $\delta\kappa_0$ renamed to $\delta\kappa$ after integration)

$$I = \int_{-\infty}^{\infty} g(\delta\kappa - \delta\kappa_0) I(\delta\kappa)\,{\rm d}\delta\kappa \quad (53)$$

$$= 1 + \underbrace{\exp\left(\frac{-B\sigma_\kappa}{\delta\kappa^2 + \sigma_\kappa^2}|\chi_{\rm ref}|\right)}_{\rm contrast} \underbrace{\cos\left[\left(\frac{B\delta\kappa}{\delta\kappa^2 + \sigma_\kappa^2} + 1\right)\chi_{\rm ref} - \varphi\right]}_{\rm measured\ phase}. \quad (54)$$

Let us summarize the result. Given a monocrystalline sample and a beam missing the Bragg condition in the crystal by $\delta\kappa$ with a distribution width of σ_κ, then the interference contrast c and the measured phase $\chi_{\rm meas}$ are given by

$$\chi_{\rm meas} = \chi_{\rm ref}\left(1 + \frac{B\delta\kappa}{\delta\kappa^2 + \sigma_\kappa^2}\right), \quad (55)$$

$$c = \exp\left(-|\chi_{\rm ref}|\frac{B\sigma_\kappa}{\delta\kappa^2 + \sigma_\kappa^2}\right), \quad (56)$$

with B depending only on crystal parameters [*cf.* equation (49)]. The orientations of beam and lattice planes with respect to the surface do not enter at all, only the orientation of beam and lattice planes to each other is important, described by $\delta\kappa$. Typical plots of contrast and diffractive phase for realistic beam divergences are shown in Fig. 5.

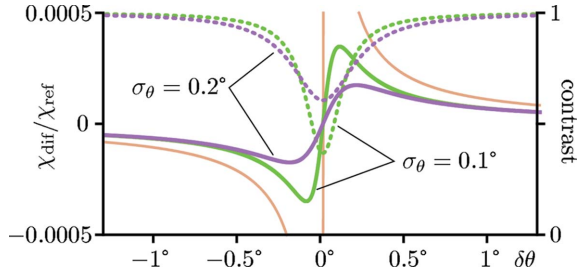

Figure 5
Relative diffractive phase (solid lines, left scale) and interference contrast (dotted lines, right scale) obtained by the convolution of the plane-wave formula (brown curve) with the angular beam distribution, calculated for two typical beam divergences σ_θ as indicated in the figure. The plot was calculated for a 220 silicon crystal of 18 mm thickness and wavelength $\lambda = 2.36$ Å. Thinner crystals would create a smaller contrast dip, but the relative diffractive phase $\chi_{\rm dif}/\chi_{\rm ref}$ would not change.

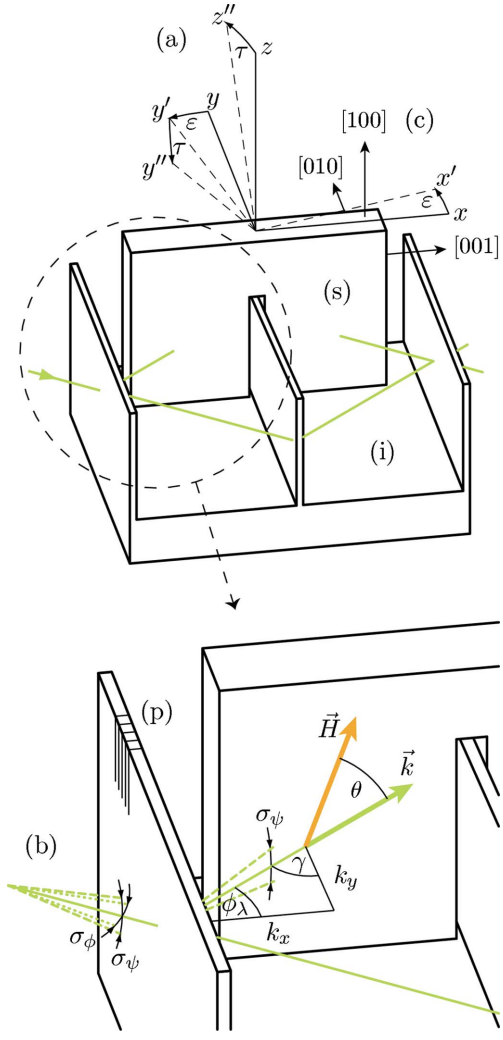

Figure 6
Setup of the sample (s) in the interferometer (i). The sample is a silicon perfect crystal with the indicated crystal orientation (c). It is aligned by rotation ε and tilt τ (a). The beam (b) enters on the left with vertical divergence σ_ψ and horizontal divergence σ_ϕ. After Bragg diffraction on the interferometer planes (p) only the vertical divergence remains for a specific wavelength while the horizontal divergence is reduced to the Darwin width.

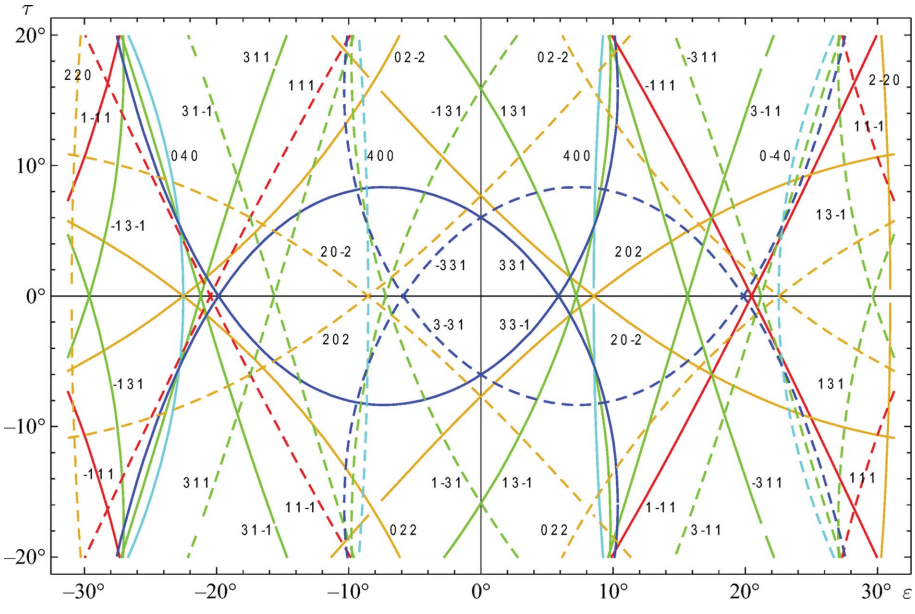

Figure 7
Bragg reflections occurring under certain sample alignment angles ε and τ and $\lambda = 2.36$ Å. The solid lines refer to the first beam transit through the sample, the dashed lines to the second transit.

The two-beam case takes only a single set of Bragg planes into account. The exact way of calculating the combined effect of n sets of Bragg planes would require an $(n+1)$-beam case. In the present approach we assume that this is necessary only in the near range close to the Bragg conditions and not in the far range where the diffractive effects are small. Then we can simply sum up the individual diffractive phases and multiply the contrast values.

3. Phase calculation for a real setup

We recently developed a new technique for high-precision scattering-length measurements by neutron interferometry (Lemmel & Wagh, 2010). The setup is shown in Fig. 6. A dual phase shifter is used which is crossed twice by the beam. Thereby the effective thickness and the resulting phase shift are doubled while the lateral beam displacement due to refraction is compensated and the interferometer is always kept focused. A nondispersive sample orientation is used (not to be confused with the nondispersive crystal orientation mentioned above) as illustrated in Fig. 6. The sample surface (s) is parallel to the lattice planes (p) of the interferometer. This way all wavelength components in the beam undergo the same phase shift (Petrascheck, 1987; Ioffe *et al.*, 1998; Vrána *et al.*, 2000; Lemmel & Wagh, 2010). Such a dual phase shifter setup allows one to create phase shifts of arbitrary magnitude, limited only by the sample thickness fitting into the interferometer.

We use a perfect crystal silicon interferometer with 220 Bragg planes and 37.91° Bragg angle, resulting in a wavelength of $\lambda = 2.36$ Å. The sample is 18 mm thick and creates a phase shift in the order of $\simeq 465 \times 2\pi$. A 10^{-5} effect means a phase change in the order of 1.7°, which is measurable with care.

3.1. Determining all possible Bragg diffractions

We locate all possible Bragg diffractions accessible by our wavelength and sample alignment angles. We denote the incident vector by $\mathbf{k}$ and the reciprocal-lattice vector in the sample by $\mathbf{H}_0$ with the Miller indices h, j, l,

$$\mathbf{k} = \begin{pmatrix} k_x \\ k_y \\ k_z \end{pmatrix}, \quad \mathbf{H}_0 = \frac{2\pi}{a_{\rm Si}} \begin{pmatrix} h \\ j \\ l \end{pmatrix}. \tag{57}$$

The crystal axes are oriented perpendicular to the sample surface [*cf.* Fig. 6 (c)]. The sample can be rotated by ε around the z axis, then by τ around the new x' axis and finally (not realized in the experiment) by ζ around the y'' axis [*cf.* Fig. 6 (a)]. The rotation turns the reciprocal-lattice vector into

$$\mathbf{H} = R_y(\zeta)\, R_x(\tau)\, R_z(\varepsilon)\, \mathbf{H}_0 \tag{58}$$

with the rotation matrices

$$R_x(\tau) = \begin{pmatrix} 1 & 0 & 0 \\ 0 & \cos\tau & -\sin\tau \\ 0 & \sin\tau & \cos\tau \end{pmatrix}, \tag{59}$$

$$R_y(\zeta) = \begin{pmatrix} \cos\zeta & 0 & -\sin\zeta \\ 0 & 1 & 0 \\ \sin\zeta & 0 & \cos\zeta \end{pmatrix}, \tag{60}$$

$$R_z(\varepsilon) = \begin{pmatrix} \cos\varepsilon & -\sin\varepsilon & 0 \\ \sin\varepsilon & \cos\varepsilon & 0 \\ 0 & 0 & 1 \end{pmatrix}. \tag{61}$$

For the accuracy needed here we neglect refraction on the sample surface and set the wavevector inside the sample equal to the one outside, $\mathbf{K} = \mathbf{k}$. Then Bragg's law in vector notation reads $\mathbf{kH} = H^2/2$ and

$$\mathbf{k} R_y(\zeta) R_x(\tau) R_z(\varepsilon) \mathbf{H}_0 = 2\pi^2 (h^2 + j^2 + l^2)/a_{\rm Si}^2. \tag{62}$$

To plot τ as a function of ε and ζ we bring the equation into the form $a \sin\tau + b \cos\tau + c = 0$ and obtain

$$\tau = 2 \arctan\left[\frac{a \pm (a^2 + b^2 - c^2)^{1/2}}{b - c}\right], \tag{63}$$

$$a = (h \sin\varepsilon + j \cos\varepsilon)(k_z \cos\zeta - k_x \sin\zeta) - l k_y, \tag{64}$$

$$b = j k_y \cos\varepsilon + l k_z \cos\zeta + h k_y \sin\varepsilon - l k_x \sin\zeta, \tag{65}$$

$$c = (h \cos\varepsilon - j \sin\varepsilon)(k_x \cos\zeta + k_z \sin\zeta) - (h^2 + j^2 + l^2)\pi/a_{\rm Si}. \tag{66}$$

Fig. 7 shows the resulting combinations of ε and τ (with $\zeta = 0$) which satisfy any Bragg condition; Fig. 8 illustrates how some of the Bragg planes are orientated in the sample. For the given wavelength of $\lambda = 2.36$ Å only the plotted reflections 111, 220, 311, 400, 331 (and their crystallographic permutations) can

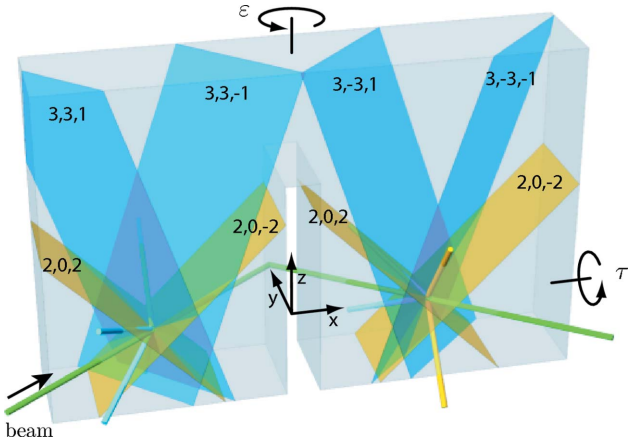

Figure 8
Illustration of some of the Bragg-plane orientations in the sample.

fully satisfy the Bragg condition. They already create quite a dense net, but the Bragg condition can be violated not only by angle but also by wavelength. Therefore we have to take even more reflections into account: 224, 333, 244 ....

At $\varepsilon = \tau = 0$ we are several degrees away from any Bragg condition and that is why we originally chose this crystal orientation. When we created the sample we already expected some influence of the Bragg planes but the detailed theory of the diffractive phase was not yet developed.

3.2. Sample and interferometer

For calculating the diffractive phase [equation (55)] and contrast loss [equation (56)] for each of the Bragg planes found above, we have to determine the Bragg deviation $\delta\kappa$ and its distribution width σ_κ. They depend on the specific geometry of the setup. Let a white beam fall onto the interferometer crystal with horizontal divergence σ_ϕ and vertical divergence σ_ψ [*cf.* Fig. 6 (b)]. The beam is Bragg diffracted by the lattice planes of the interferometer crystal [*cf.* Fig. 6 (p)]. Thereby the beam divergence remains the same but the wavelength is set to $\lambda = 2d_{\rm IFM}\sin\phi$ and we can write the beam incident on the sample as

$$\mathbf{k} = k\begin{pmatrix}\cos\phi\cos\psi\\ \sin\phi\cos\psi\\ \sin\psi\end{pmatrix}, \quad k = \frac{\pi}{d_{\rm IFM}\sin\phi}, \tag{67}$$

where $d_{\rm IFM}$ denotes the lattice constant of the diffracting Bragg planes of the interferometer crystal. When the beam is refracted on the sample surface (with surface normal $\mathbf{n}$) its component normal to the surface is shortened to $[(\mathbf{kn})^2 - k^2 v_0]^{1/2} \simeq \mathbf{kn} - k^2 v_0/(2\mathbf{kn})$ and the refracted wavevector $\boldsymbol{\kappa}$ inside the sample reads

$$\boldsymbol{\kappa} = \mathbf{k} - \frac{v_0 k^2}{2\mathbf{kn}}\mathbf{n}, \quad \mathbf{n} = \begin{pmatrix}\sin\varepsilon\\ -\cos\varepsilon\cos\tau\\ -\cos\varepsilon\sin\tau\end{pmatrix}. \tag{68}$$

We calculate the misset parameter $\delta\kappa$ [equation (38)] for a particular set of Bragg planes defined by equation (58). The distribution width σ_κ is calculated from the four extreme $\delta\kappa$ values within the beam divergence $\delta\kappa_{\pm_1\pm_2} = \delta\kappa(\phi \pm_1 \sigma_\phi, \psi \pm_2 \sigma_\psi)$,

$$\delta\kappa = \frac{|\boldsymbol{\kappa}\mathbf{H}|}{H^2} - \frac{1}{2}, \tag{69}$$

$$\sigma_\kappa = \Big\{\big[(\delta\kappa - \delta\kappa_{++})^2 + (\delta\kappa - \delta\kappa_{+-})^2 + (\delta\kappa - \delta\kappa_{-+})^2 + (\delta\kappa - \delta\kappa_{--})^2\big]/4\Big\}^{1/2}. \tag{70}$$

Alternatively, obtaining virtually the same numerical results, we can calculate σ_κ by error propagation from a Gaussian distribution,

$$\sigma_\kappa = \left[\left(\frac{\partial\delta\kappa}{\partial\phi}\,\sigma_\phi\right)^2 + \left(\frac{\partial\delta\kappa}{\partial\psi}\,\sigma_\psi\right)^2\right]^{1/2}. \tag{71}$$

For perfect alignment $\varepsilon = \tau = \zeta = 0$ we have

$$\delta\kappa = \frac{\left|h\cot\phi\cos\psi + j\cos\psi - j(V_0 m d_{\rm IFM}^2/\pi^2\hbar^2\cos\psi) + l(\sin\psi/\sin\phi)\right|}{2(h^2+j^2+l^2)d_{\rm IFM}/a_{\rm Si}} - \frac{1}{2} \tag{72}$$

and for $\psi = 0$ the distribution width amounts to

$$\sigma_\kappa = \frac{a_{\rm Si}(h^2\sigma_\phi^2 + l^2\sigma_\psi^2\sin^2\phi)^{1/2}}{2(h^2+j^2+l^2)d_{\rm IFM}\sin^2\phi}. \tag{73}$$

3.3. Experiment

The experimental data were collected in May 2011 at the neutron interferometry setup S18 at the Institute Laue–Langevin in Grenoble. At that time the detailed theory was not yet developed and therefore the data are more explorative than analytical in nature. We scanned the tilt angle τ for several values of rotation angle ε and recorded for each sample orientation a full interferogram with an auxiliary phase flag. As the sample had been designed to be as thick as possible it could be rotated and tilted only up to 10° but it was enough to access a few Bragg diffractions (*cf.* Fig. 7).

The observed interference contrast and phase are plotted in Figs. 9(*a*) and 9(*b*), respectively. The contrast shows significant dips at certain alignment angles which are summarized by the dots in Fig. 10(*a*). They fit perfectly to the locations where Bragg diffraction is expected if we assume a slight misalignment of the sample crystal axes with respect to the sample surface of $\delta\varepsilon = -0.2°$, $\delta\tau = -0.3°$, $\delta\zeta = -0.6°$. The magnitude of these values agrees very well with the accuracy of the sample manufacturing. The values are effective values and might also include a ζ offset of the sample holder and a small vertical component of the main beam, $\psi \neq 0$.

Having determined the crystal misalignment angles we calculate the expected contrast reduction. We calculate the contribution from all sets of Bragg planes and multiply them together. Fig. 10(*b*) shows the resulting contrast in an ε/τ map, Fig. 9(*a*) compares it with the measured data. In

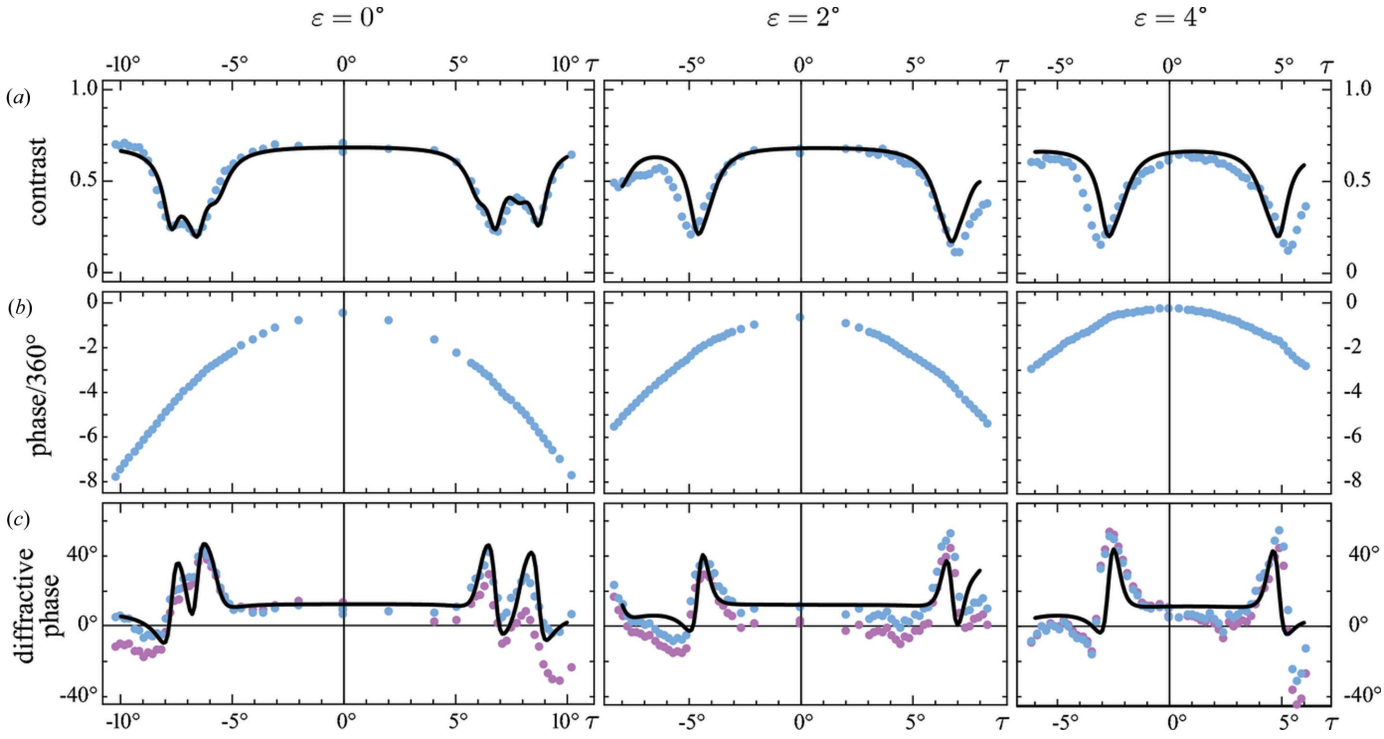

Figure 9
Calculated values (curves) compared to the experimental data (dots) which have been recorded *versus* sample tilt τ for different rotation angles ε. The interference contrast (*a*) shows significant dips at the locations of Bragg diffraction (*cf.* Fig. 10*a*). The phase (*b*) shows the typical $1/\cos\tau$ behaviour. The deviation from a simple $1/\cos\tau$ fit is shown by the red dots in (*c*). The features of the diffractive phase can already be recognized qualitatively. A more sophisticated data analysis (which requires a good value of the scattering length to be already known, see text) provides a more accurate extraction of the refractive phase shown by the blue dots.

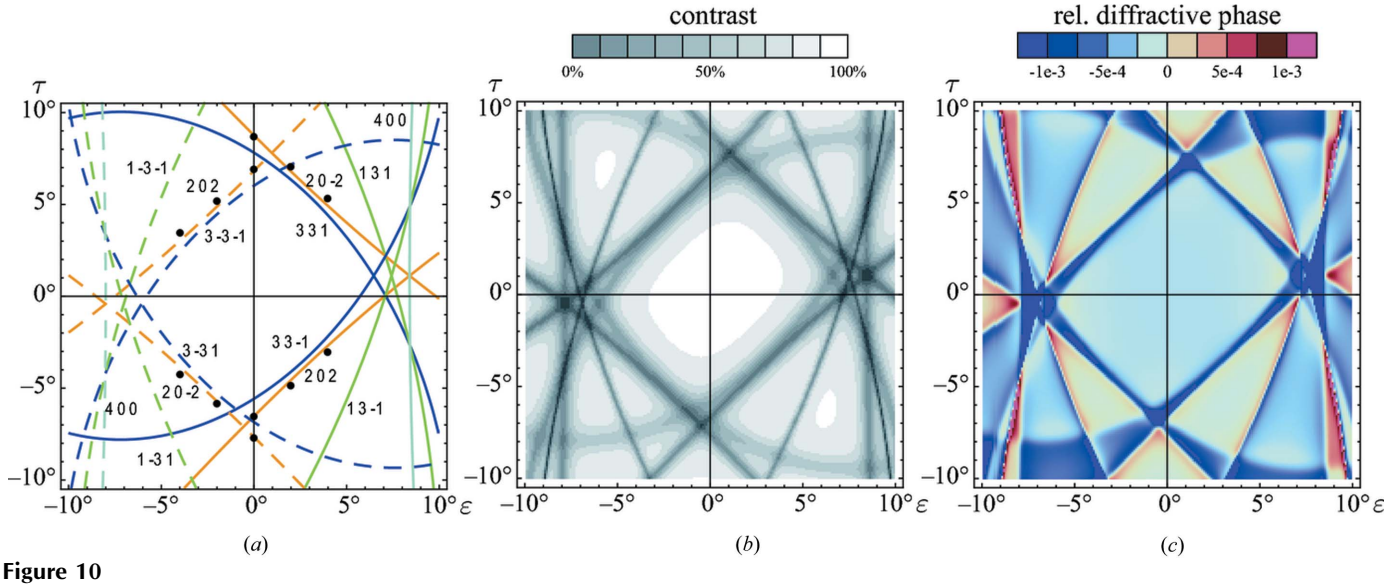

Figure 10
(*a*) Location of Bragg reflections in the alignment space of sample rotation ε and sample tilt τ. The crystal orientation has been slightly adjusted with respect to the crystal surface ($\delta\varepsilon = -0.2^\circ$, $\delta\tau = -0.5^\circ$, $\delta\zeta = -0.5^\circ$) such that the lines of Bragg diffraction pass through the measured points of lowest contrast (dots). (*b*) Calculated contrast map. (*c*) Calculated relative diffractive phase.

the latter plot the calculated values have been multiplied by the intrinsic interferometer contrast (sample-out contrast) of 0.7. A good agreement was found for a beam divergence of $\sigma_\phi = 0.1^\circ$ and $\sigma_\psi = 0.2^\circ$. In the setup the divergence was defined by two slits of width × height = 20 × 43 and 3 × 4 mm, respectively, in a distance of 1160 mm, giving rise to trapezoidal distributions with an $\mathrm{FWHM}_\phi = 0.25^\circ$ and $\mathrm{FWHM}_\psi = 0.53^\circ$. We do not know how to exactly translate these widths into the Lorentzian σ of our model but the agreement seems reasonably good.

Table 1
Comparison of the contributions of different sets of Bragg planes to the phase and the contrast measured with the well aligned sample ($\varepsilon = \tau = 0$).

Each line of the table summarizes the effects of several similar sets of planes indicated in the first two columns. The contrast and phase values (last three columns) are the combined result of these planes, the values of $\delta\theta$, κ, $\delta\kappa$ and σ_κ are averaged. [The individual values of the latter are nearly but not exactly the same due to the slight misalignment of the crystal axes to the sample surface, *i.e.* the asymmetry of Fig. 10(*a*) compared to Fig. 7.] The table is sorted by the modulus of $\delta\theta$ which corresponds to the distance of the curves in Figs. 7 and 10(*a*) from the centre. $\delta\theta$ is undefined for the planes 442, 242 *etc.* because the corresponding Bragg condition can only be fulfilled by a shorter wavelength. However, only $\delta\kappa$ is of importance for the calculation.

Planes of first transit	Planes of second transit	$\delta\theta$	κ/H	$\delta\kappa$	$\sigma_\kappa\,(10^{-3})$	$B\,(10^{-6})$	Contrast	$\chi_{\rm rel}\,(10^{-6})$	$\chi_{\rm dif}$ (°)
331, 33$\bar{1}$	33$\bar{1}$, $\bar{3}$31	3.87	0.528	0.0103	0.896	0.256	0.987	102.0	−8.34
202, 20$\bar{2}$	202, 20$\bar{2}$	−4.09	0.814	−0.0471	2.07	1.22	0.993	−107.0	8.80
131, 13$\bar{1}$	1$\bar{3}$1, $\bar{1}$31	6.61	0.694	0.0521	0.757	0.442	0.999	34.9	−2.86
400	400	−8.42	0.576	−0.0471	1.31	0.608	0.999	−26.5	2.18
$\bar{3}$11, 3$\bar{1}$1	311, 31$\bar{1}$	−14.4	0.694	−0.135	1.54	0.442	1.00	−13.3	1.09
02$\bar{2}$, 022	022, 02$\bar{2}$	−12.0	0.814	−0.145	1.61	1.22	0.999	−33.3	2.73
1$\bar{1}$1, $\bar{1}$11	111, 11$\bar{1}$	−16.5	1.33	−0.370	2.76	1.62	1.00	−17.7	1.46
311, 31$\bar{1}$	$\bar{3}$11, 3$\bar{1}$1	17.8	0.694	0.123	1.54	0.442	1.00	14.3	−1.17
113, 11$\bar{3}$	$\bar{1}$13, 1$\bar{1}$3	−21.0	0.694	−0.206	1.82	0.442	1.00	−8.58	0.705
040	040	−22.2	0.576	−0.145	0.00969	0.608	1.00	−8.31	0.682
$\bar{1}$31, 1$\bar{3}$1	13$\bar{1}$, $\bar{1}$31	−27.4	0.694	−0.277	0.750	0.442	1.00	−6.33	0.520
313, 31$\bar{3}$	3$\bar{1}$3, $\bar{3}$13	−28.1	0.528	−0.139	1.31	0.256	1.00	−7.39	0.606
22$\bar{0}$	2$\bar{2}$0	−31.0	0.814	−0.402	1.30	1.22	1.00	−6.09	0.500
111, 11$\bar{1}$	$\bar{1}$11, 1$\bar{1}$1	32.1	1.33	0.577	2.77	1.62	1.00	11.2	−0.923
133, 13$\bar{3}$	1$\bar{3}$3, $\bar{1}$33	−34.0	0.528	−0.180	1.05	0.256	1.00	−5.66	0.464
1$\bar{1}$3, $\bar{1}$13	113, 11$\bar{3}$	−43.1	0.694	−0.464	1.82	0.442	1.00	−3.82	0.313
220	2$\bar{2}$0	45.2	0.814	0.308	1.31	1.22	1.00	7.91	−0.649
$\bar{3}$13, 3$\bar{1}$3	313, 31$\bar{3}$	−47.6	0.528	−0.289	1.31	0.256	1.00	−3.56	0.292
$\bar{1}$33, 1$\bar{3}$3	133, 13$\bar{3}$	−57.1	0.528	−0.371	1.05	0.256	1.00	−2.75	0.226
004	004	−59.7	0.576	−0.493	1.61	0.608	1.00	−2.46	0.202
$\bar{3}$31, 3$\bar{3}$1	331, 33$\bar{1}$	−64.5	0.528	−0.438	0.890	0.256	1.00	−2.35	0.193
422, 42$\bar{2}$	4$\bar{2}$2, $\bar{4}$22		0.470	−0.0797	1.02	0.405	1.00	−20.4	1.68
242, 24$\bar{2}$	2$\bar{4}$2, $\bar{2}$42		0.470	−0.112	0.693	0.405	1.00	−14.4	1.18
224, 22$\bar{4}$	2$\bar{2}$4, $\bar{2}$24		0.470	−0.231	1.16	0.405	1.00	−7.03	0.577
4$\bar{2}$2, $\bar{4}$22	422, 42$\bar{2}$		0.470	−0.316	1.02	0.405	1.00	−5.15	0.423
2$\bar{4}$2, $\bar{2}$42	242, 24$\bar{2}$		0.470	−0.414	0.689	0.405	1.00	−3.90	0.320
22$\bar{4}$, $\bar{2}$24	224, 22$\bar{4}$		0.470	−0.467	1.16	0.405	1.00	−3.48	0.285
333, 33$\bar{3}$	33$\bar{3}$, $\bar{3}$33		0.443	−0.141	0.922	0.180	1.00	−5.11	0.420
33$\bar{3}$, $\bar{3}$33	333, 33$\bar{3}$		0.443	−0.457	0.920	0.180	1.00	−1.58	0.130
Total							0.976	−146.0	12.0

The calculated total diffractive phase is shown in Fig. 10(*c*) in an ε/τ map and in Fig. 9(*c*) in comparison with the experimental data. In a first approach of data evaluation we ignore the diffractive phase. We fit the measured phase (Fig. 9*b*) by the refractive formula

$$\chi_{\rm ref}(\varepsilon,\tau) = \chi_{\rm ref0}\frac{1}{\cos\tau}\frac{1}{2}\left[\frac{\sin\phi}{\sin(\phi+\varepsilon)}+\frac{\sin\phi}{\sin(\phi-\varepsilon)}\right] \qquad (74)$$

given *e.g.* in Lemmel & Wagh (2010) and then subtract the measured data from the fit. The result is shown by the red dots in Fig. 9(*c*) and already shows some qualitative agreement with the theory. In a second approach we first subtract the calculated diffractive phase from the measured phase and then fit the refractive phase. The difference between the measured data and this fit is shown by the blue dots and agrees much better with the theory. In a measurement of the coherent scattering length, where $\chi_{\rm ref}$ has to be determined by the fit, one should iterate this process because $\chi_{\rm ref}$ is already needed to calculate $\chi_{\rm dif}$.

Because of limited experimental time the intrinsic interferometer phase (sample-out phase) was not recorded and subtracted. This means that the phase curves (Fig. 9*b*) have a random offset. Only their shape is significant and even that might have been distorted due to phase drifts induced by the environment during the measurement process. However, the positive and the negative τ sides have been recorded in separate runs. First all positive τ were recorded for the different values of ε, then all negative sides, taking several days in total. The fact that the two sides fit nearly seamlessly together at $\tau = 0$ shows that the phase drift was reasonably small.

4. Discussion

As one can see in Fig. 10 the diffractive effects are quite strong for some Bragg planes, *e.g.* 20 ± 2, and much weaker for other ones, *e.g.* $3 \pm 3 \pm 1$, which create only a weak shadow in Figs. 10(*b*) and 10(*c*). Table 1 compares the influence of the different Bragg planes on the phase measured at $\varepsilon = \tau = 0$. The table includes the Bragg-angle deviation $\delta\theta$ for convenience although the relevant deviation parameter for the diffractive phase is $\delta\kappa$. If we sum up only the contributions of the Bragg planes with relatively 'small' Bragg-angle deviations, *e.g.* $|\delta\theta| < 10^\circ$, we need only the first four lines of the table and end up with a diffractive phase of -0.23°. We should however look at $\delta\kappa$, otherwise we would overlook planes which can only be accessed by a wavelength change. We could limit ourselves *e.g.* to $|\delta\kappa| < 0.1$ and take the first four lines plus

the 442 line, in which case the diffractive phase would amount to 1.45°. However, if we sum up all planes listed in the table, we end up with $\chi_{\rm dif} = 12.0°$ ($\chi_{\rm rel} = -1.5 \times 10^{-4}$) without even getting a clear indication of convergence of the sum. Although the additional contributions become smaller and smaller, nearly all of them have the same sign and push $\chi_{\rm dif}$ to an increasingly larger value. As a result we get a phase offset which is constant over the angular range of the alignment scans and which cannot be distinguished experimentally from the refractive phase itself (*cf.* Fig. 9*c*). Consequently, the precision of the scattering-length measurement depends crucially on the reliability of the theoretical calculation. Our calculation is based on the incoherent sum of two-beam cases which is strictly speaking only correct for combining the first and the second sample transit. Within each transit the contributions of all Bragg reflections should be added coherently, requiring an n-beam case of dynamical diffraction with n in the order of 10. Such a calculation for arbitrary Bragg-plane orientations and large Bragg-angle deviations is quite challenging. As a first step in future work we aim to investigate the three-beam case, to get at least an idea of the magnitude of the cross terms.

However, phase corrections in the order of $\lesssim 10^{-4}$ are not totally unexpected. The phase formula [equation (1)], $\chi = -\lambda N b_c D$, follows from the kinematic scattering theory as well as from the one-beam approximation of the dynamical theory. In both cases multiple scattering is neglected. A more rigorous model has been developed by Sears (1982, 1985) for isotropic media (liquids, gases) yielding two correction terms:

$$\chi = -\lambda N b_c D\left(1 + J' + \frac{\lambda^2 N b_c}{4\pi}\right). \qquad (75)$$

J' is the local field correction which takes multiple scattering into account and the λ^2 correction term originates from diffuse scattering. If we assume silicon to be isotropic, *i.e.* a liquid with the number density of the real crystal, then J' would be in the order of 10^{-5} and the λ^2 term in the order of 10^{-6}. J' can be positive or negative depending on the wavelength and the nearest-neighbour distance in the liquid. Our calculation for the single crystal of silicon uses the theory of dynamical diffraction which already includes multiple scattering in its fundamental equations, since the Schrödinger equation of the neutron is solved on the periodic potential of the whole crystal. An n-beam approximation with $n < \infty$ reduces the completeness such that only certain multiple scattering processes are taken into account. Nevertheless a remaining correction term equivalent to the local field correction should be expected, except for the one-beam case. Fig. 11 shows our calculated phase correction for a wide range of crystal orientations. Again the Bragg condition lines of Fig. 7 are reproduced. The rather constant regions between the lines have varying values of positive or negative sign (red and blue, respectively). As for the isotropic model, there is no constant correction term for the whole sample but only for a specific experimental situation depending on the incident beam and the spatial configuration of the scatterers.

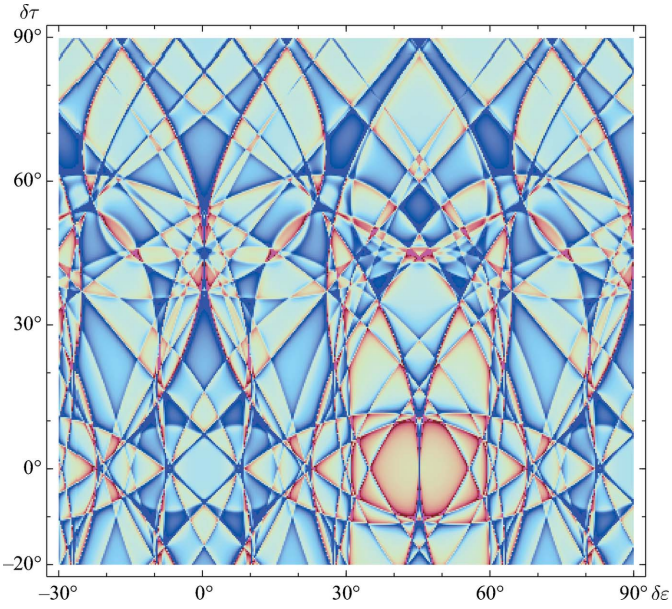

Figure 11
Relative diffractive phase calculated for a wide range of crystal orientation angles. The sample surfaces are kept constant ($\varepsilon = \tau = 0$) but the inner crystal structure is rotated by $\delta\varepsilon$ and $\delta\tau$. The colour shading is the same as in Fig. 10(*c*). The lower left part of the map covers the angular range of Fig. 7.

5. Summary and conclusion

Based on the dynamical diffraction theory of neutrons, we have comprehensively worked out the two-beam case for arbitrary Bragg-plane orientations and arbitrary deviations from the Bragg condition (for non-absorbing materials). We investigated the influence of Bragg diffraction on the phase of the transmitted beam and furthermore on the interference contrast in a neutron interferometry measurement. The theory agrees very well with experimental data. If scattering-length measurements are performed on single-crystal samples the crystal orientation has to be chosen carefully so that the beam direction is at least a few degrees away from any Bragg condition.

Open questions remain as concerns high-precision measurements. If the phase can be measured with 10^{-4} or higher accuracy, the diffractive phase is non-negligible for Bragg-angle deviations of up to several degrees. In this regime there are always several Bragg reflections within reach. All Bragg planes together create a non-vanishing correction to the refractive phase which we interpret as a local field effect. Further work on the n-beam case is necessary to confirm that our method of incoherently summing up the individual two-beam cases is an accurate approximation.

APPENDIX *A*
Exact solution of the two-beam case

We derive the exact solution of the two-beam case for arbitrary Bragg-plane orientation and arbitrarily large deviations from the Bragg condition. The geometry is illustrated in Fig.

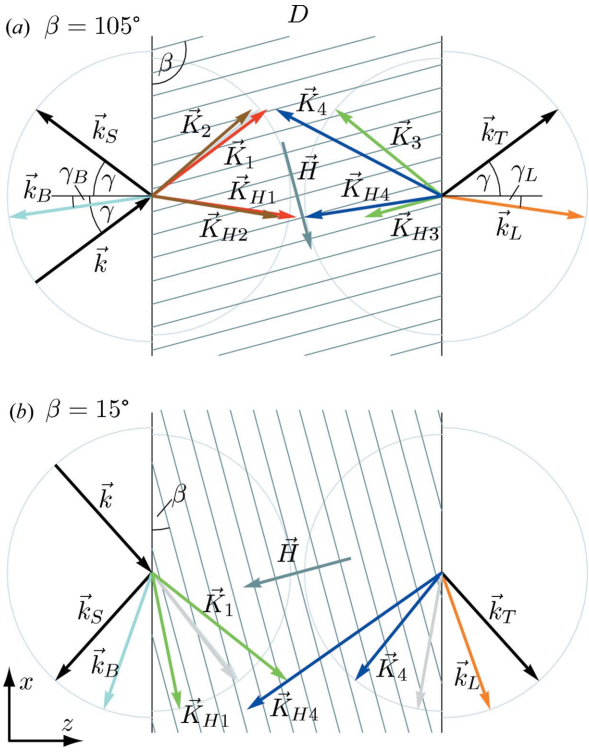

Figure 12
The wavevectors inside and outside the crystal for the asymmetric Laue case (*a*) and asymmetric Bragg case (*b*), calculated for $V_0/E = 0.09$.

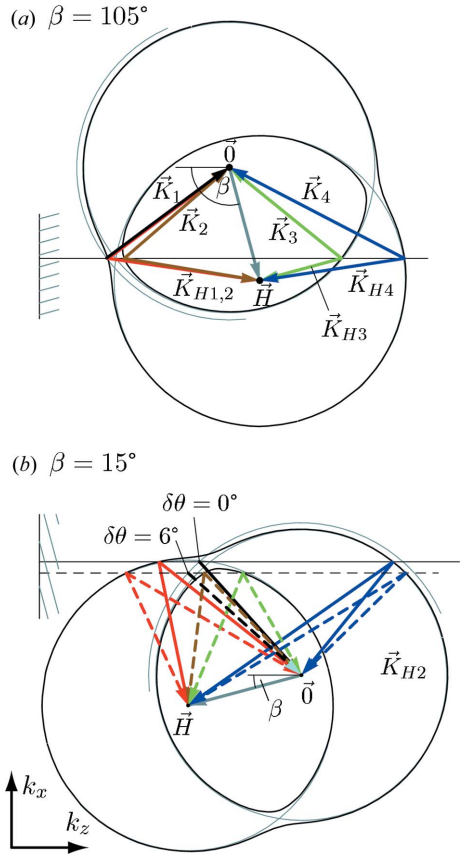

Figure 13
Graphical solution of equation (5) in reciprocal space, plotted for $V_0/E = 0.09$. The dispersion surfaces (black) approach circles (thin lines) around **0** and **H** and represent all possible values of **K** and $\mathbf{K}_H$ allowed by the Schrödinger equation in the two-beam case. The solutions (coloured) for a particular incident vector **k** (black) are given by the intersection points of the dispersion surface and the surface normal through the vector **k**'s tail. **k**'s tip always points to **0**. Part (*a*) shows the Laue case, (*b*) the Bragg case. Part (*b*) shows both the situation of exact Bragg compliance $\delta\theta = 0$ (solid lines) and misalignment by $\delta\theta = 6^\circ$ (dashed lines). The former has only two real solutions (red and blue). The other two solutions are complex, leading to total reflection.

12. We assume a crystal slab with parallel surfaces perpendicular to the z axis and with thickness D. The reciprocal-lattice vector **H** lies in the x/z plane. Any y component of the incident wavevector **k** can be ignored, as it is neither affected by the crystal surface (being tangential) nor by the lattice planes (being perpendicular to **H**). Thus all wavevectors also lie in the x/z plane.

There are four wavevectors leaving the crystal (Fig. 12): the surface reflected component $\mathbf{k}_S$, the transmitted component $\mathbf{k}_T$, the diffracted component $\mathbf{k}_B$ exiting on the front surface (Bragg case) and the diffracted component $\mathbf{k}_L$ exiting on the back surface (Laue case). In principle both Bragg and Laue components appear simultaneously if surface reflection is taken into account. For example, in the Laue case a small component is reflected on the back surface of the crystal, travels back to the front surface and leaves the crystal with $\mathbf{k}_B$,

$$\mathbf{k}_S = \begin{pmatrix} k_x \\ -k_z \end{pmatrix}, \quad \mathbf{k}_T = \begin{pmatrix} k_x \\ k_z \end{pmatrix}, \tag{76}$$

$$\mathbf{k}_B = \begin{pmatrix} k_x + H_x \\ -k_{Lz} \end{pmatrix}, \quad \mathbf{k}_L = \begin{pmatrix} k_x + H_x \\ k_{Lz} \end{pmatrix}, \tag{77}$$

$$k_{Lz} = [k^2 - (k_x + H_x)^2]^{1/2}. \tag{78}$$

The components of these vectors follow from the fact that the x component is preserved on all surfaces and can be changed only by H_x inside the crystal. The z component is actually split into different parts inside the crystal (see next section) but for a crystal slab with parallel surfaces they always recombine to a single component outside the crystal (Batterman & Cole, 1964). The z component can be inverted on either surface, therefore $k_{Bz} = -k_{Lz}$, and the energy has to be conserved, giving the value of k_{Lz} [equation (78)].

A1. *K* vectors inside the crystal

The basic equation of the two-beam case is the quartic equation given by equation (5). Its graphical representation is the well known dispersion surfaces shown in Fig. 13. Here we solve the quartic equation analytically (Dickson, 1914 and WolframMathWorld, http://mathworld.wolfram.com/QuarticEquation.html). Brought into the form

$$0 = \overline{K}_z^4 + a_3\overline{K}_z^3 + a_2\overline{K}_z^2 + a_1\overline{K}_z + a_0, \tag{79}$$

$$a_3 = 2\overline{H}_z, \tag{80}$$

$$a_2 = \overline{H}^2 + 2\overline{H}_x\overline{k}_x - 2\overline{\kappa}_z^2 = \overline{H}_z^2 - \overline{k}_{Lz}^2 + v_0 - \overline{\kappa}_z^2, \tag{81}$$

$$a_1 = -2\overline{H}_z\overline{\kappa}_z^2, \tag{82}$$

$$a_0 = -\overline{\kappa}_z^2\left(\overline{H}^2 + 2\overline{H}_x\overline{k}_x - \overline{\kappa}_z^2\right) - |v_H|^2 \tag{83}$$

$$= -\overline{\kappa}_z^2\left(\overline{H}_z^2 - \overline{k}_{Lz}^2 + v_0\right) - |v_H|^2, \tag{84}$$

it has the following four solutions:

$$\overline{K}_z = \begin{cases} -b_3 \pm_1 (g+u)^{1/2} \pm_2 \{2g - u \pm_1 [f/(g+u)^{1/2}]\}^{1/2}, & g+u \neq 0, \\ -b_3 \pm_2 [3g \pm_1 (f_0)^{1/2}]^{1/2}, & g+u = 0, \end{cases} \tag{85}$$

$$b_0 = \frac{a_0}{4},\ b_1 = \frac{a_1}{8},\ b_2 = \frac{a_2}{12},\ b_3 = \frac{a_3}{4}, \tag{86}$$

$$g = -2b_2 + b_3^2, \tag{87}$$

$$f = -2b_1 + b_3(6b_2 - 2b_3^2), \tag{88}$$

$$f_0 = -4b_0 + (6b_2 - 2b_3^2)^2, \tag{89}$$

$$u = [v - (v^2 - w^3)^{1/2}]^{1/3} + [v + (v^2 - w^3)^{1/2}]^{1/3} \tag{90}$$

$$= [v - (v^2 - w^3)^{1/2}]^{1/3} + \frac{w}{[v - (v^2 - w^3)^{1/2}]^{1/3}}, \tag{91}$$

$$v = b_2^3 - b_2(b_0 + b_1b_3) + \tfrac{1}{2}(b_1^2 + b_0b_3^2), \tag{92}$$

$$w = b_2^2 + \tfrac{1}{3}(b_0 - 2b_1b_3). \tag{93}$$

The solutions are shown in Fig. 14 for different parameters. The two independent plus–minus signs $\pm_1$ and $\pm_2$ in equation (85) create the four different solutions. To get continuous functions for $\overline{K}_z(\beta)$ we do not assign fixed numbers to certain plus–minus branches. Instead we sort the solutions by their real value. Otherwise *e.g.* the red and the green curves in Fig. 14(*b*) would exchange their values in the range $0 < \beta \lesssim 35°$. Every quartic equation (79) with real parameters a_n has at least two real solutions, in our case $\overline{K}_{z1}$ and $\overline{K}_{z4}$. These solutions lie on the outer dispersion surface in Fig. 13. The other two solutions might become complex, in which case they are complex conjugates. This corresponds to the total reflection of the Bragg case where there is no intersection between the surface normal and the inner dispersion surface (*cf.* Fig. 13*b*). The imaginary part is plotted with dashed lines in Fig. 14.

We checked the numerical stability of equations (85)–(93) by feeding the calculated values of $\overline{K}_z$ for the silicon sample into numerical 'root polishing' algorithms for polynomial equations (Press *et al.*, 2002). These algorithms (*e.g.* Laguerre's method) change the given root value by trial and error until the original equation is best fulfilled. The roots slightly changed their values by $|\delta\overline{K}_z/\overline{K}_z| \lesssim 10^{-9}$. We used a PC with 80 bit floating-point accuracy, *i.e.* 64 bit mantissa or about 19 significant decimal digits.

The solutions of the quartic equation of the form in equation (79) fulfil certain relations known as Vieta's formulas (WolframMathWorld). We will need them later on to simplify results.

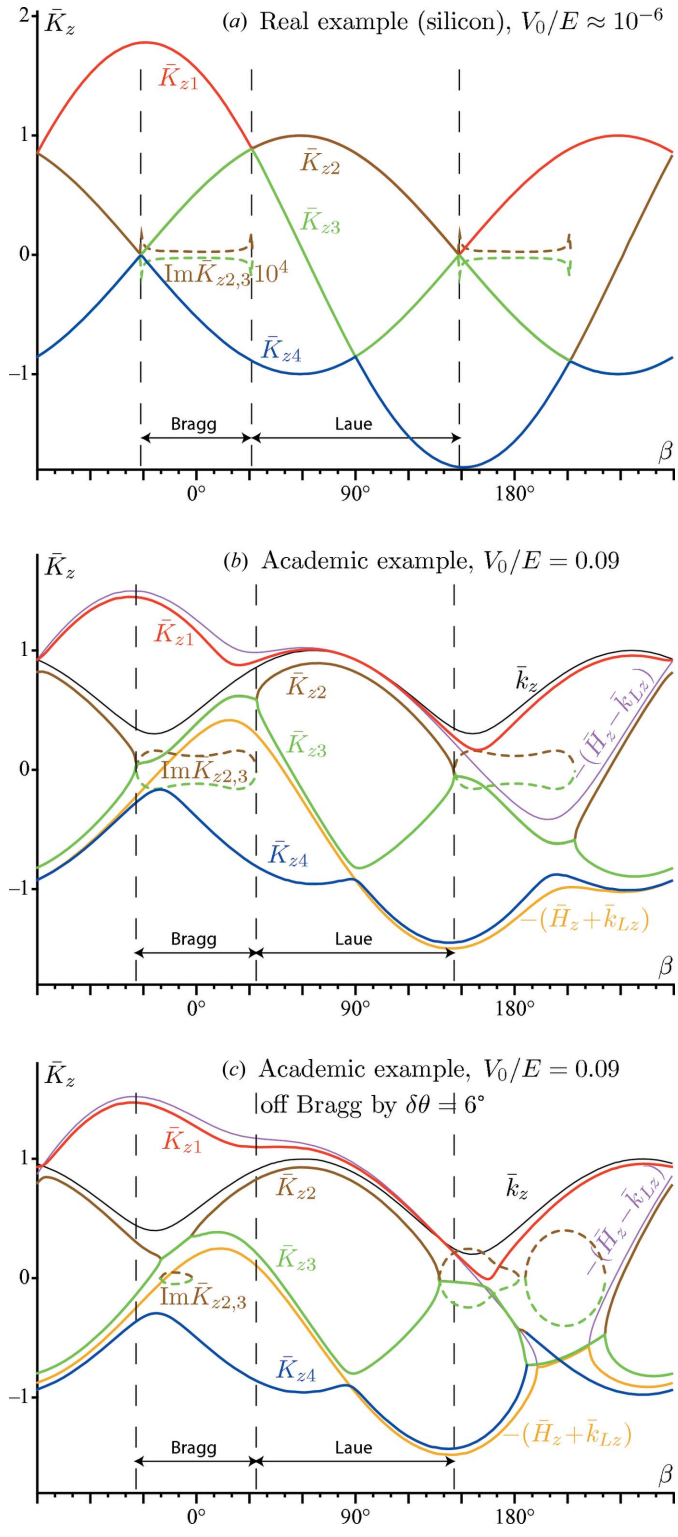

Figure 14
Solutions $\overline{K}_{z1}$ to $\overline{K}_{z4}$ as a function of the lattice-plane orientation β. The incidence vector is adjusted accordingly to always fulfil the Bragg condition in plots (*a*) and (*b*) and to be off-Bragg by 6° in plot (*c*). Plot (*a*) is calculated for a real silicon sample where some solutions are so close to each other that they cannot be distinguished in the plot. Plots (*b*) and (*c*) are calculated for a hypothetical material with much stronger neutron potential to illustrate the qualitative behaviour of the solutions. Non-vanishing imaginary parts are shown by dashed lines.

$$\overline{K}_{z1}+\overline{K}_{z2}+\overline{K}_{z3}+\overline{K}_{z4}=-a_3, \tag{94}$$

$$\overline{K}_{z1}\overline{K}_{z2}+\overline{K}_{z1}\overline{K}_{z3}+\overline{K}_{z1}\overline{K}_{z4}+\overline{K}_{z2}\overline{K}_{z3}+\overline{K}_{z2}\overline{K}_{z4}+\overline{K}_{z3}\overline{K}_{z4}=a_2, \tag{95}$$

$$\overline{K}_{z1}\overline{K}_{z2}\overline{K}_{z3}+\overline{K}_{z2}\overline{K}_{z3}\overline{K}_{z4}+\overline{K}_{z3}\overline{K}_{z4}\overline{K}_{z1}+\overline{K}_{z4}\overline{K}_{z1}\overline{K}_{z4}=-a_1, \tag{96}$$

$$\overline{K}_{z1}\overline{K}_{z2}\overline{K}_{z3}\overline{K}_{z4}=a_0. \tag{97}$$

Further useful equations can be drived from Vieta's formulas.

$$\overline{K}_{z1}^2+\overline{K}_{z2}^2+\overline{K}_{z3}^2+\overline{K}_{z4}^2=-2a_2+a_3^2, \tag{98}$$

$$(\overline{K}_{z1}^2-\overline{\kappa}_z^2)(\overline{K}_{z2}^2-\overline{\kappa}_z^2)(\overline{K}_{z3}^2-\overline{\kappa}_z^2)(\overline{K}_{z4}^2-\overline{\kappa}_z^2)=|v_H|^4, \tag{99}$$

$$(\overline{K}_{z1}+\overline{k}_z)(\overline{K}_{z2}+\overline{k}_z)(\overline{K}_{z3}+\overline{k}_z)(\overline{K}_{z4}+\overline{k}_z)=\left[(\overline{H}_z-\overline{k}_z)^2-\overline{k}_{\mathrm{L}z}^2\right]v_0+v_0^2-|v_H|^2. \tag{100}$$

A2. Amplitudes

Having determined all wavevectors we can make an ansatz for the wave functions in the three sections before, inside and behind the crystal slab.

$$\psi_{\mathrm{I}}=\exp(i\mathbf{kr})+b\exp(i\mathbf{k}_{\mathrm{B}}\mathbf{r})+s\exp(i\mathbf{k}_{\mathrm{S}}\mathbf{r}),\quad z\le 0, \tag{101}$$

$$\psi_{\mathrm{II}}=\sum_{n=1}^{4}\left\{u_n\exp(i\mathbf{K}_n\mathbf{r})+u_{Hn}\exp[i(\mathbf{K}_n+\mathbf{H})\mathbf{r}]\right\},\quad 0\le z\le D, \tag{102}$$

$$\psi_{\mathrm{III}}=t\exp(i\mathbf{kr})+l\exp(i\mathbf{k}_{\mathrm{L}}\mathbf{r}),\quad D\le z. \tag{103}$$

t and s denote the transmitted and surface-reflected amplitudes, respectively, b and l the diffracted amplitudes for the Bragg and Laue cases, respectively (*cf.* Fig. 12). u_n and u_{Hn} denote the eight amplitudes inside the crystal. As u_{Hn} can be expressed by u_n using equation (2)

$$u_{Hn}=u_n(\overline{\kappa}_z^2-\overline{K}_{zn}^2)/v_{-H} \tag{104}$$

there remain eight unknown quantities: s, b, t, l, u_1, u_2, u_3, u_4. We have four matching conditions on the surfaces:

$$\psi_{\mathrm{I}}=\psi_{\mathrm{II}}|_{z=0},\qquad \partial_z\psi_{\mathrm{I}}=\partial_z\psi_{\mathrm{II}}|_{z=0}, \tag{105}$$

$$\psi_{\mathrm{II}}=\psi_{\mathrm{III}}|_{z=D},\qquad \partial_z\psi_{\mathrm{II}}=\partial_z\psi_{\mathrm{III}}|_{z=D}. \tag{106}$$

These equations are sufficient because each of them splits into two independent parts. For example, $\psi_{\mathrm{I}}=\psi_{\mathrm{II}}|_{z=0}$ gives

$$\left\{1+s-\sum_n u_n\right\}+\exp(iH_x x)\left[b-\sum_n u_{H_n}\right]=0. \tag{107}$$

To be valid for all x the braced and the bracketed terms have to vanish independently, giving two equations. Linear combination of all eight equations gives the following simplified system of equations, using the abbreviations

$$\kappa_n^2=\kappa_z^2-K_{zn}^2,\qquad \overline{\kappa}_n^2=\kappa_n^2/k^2, \tag{108}$$

$$k_n^{\pm}=k_z\pm K_{zn},\qquad \overline{k}_n^{\pm}=k_n^{\pm}/k, \tag{109}$$

$$h^{\pm}=H_z\pm k_{\mathrm{L}z},\qquad \overline{h}^{\pm}=h^{\pm}/k, \tag{110}$$

$$h_n^{\pm}=H_z\pm k_{\mathrm{L}z}+K_{zn},\qquad \overline{h}_n^{\pm}=h_n^{\pm}/k, \tag{111}$$

$$\begin{pmatrix}
1 & 1 & 1 & 1 & -1 & 0 & 0 & 0\\
\overline{K}_{z1} & \overline{K}_{z2} & \overline{K}_{z3} & \overline{K}_{z4} & \overline{k}_z & 0 & 0 & 0\\
\overline{K}_{z1}^2 & \overline{K}_{z2}^2 & \overline{K}_{z3}^2 & \overline{K}_{z4}^2 & -\overline{\kappa}_z^2 & v_{-H} & 0 & 0\\
\overline{K}_{z1}^3 & \overline{K}_{z2}^3 & \overline{K}_{z3}^3 & \overline{K}_{z4}^3 & \overline{k}_z\overline{\kappa}_z^2 & -v_{-H}\overline{h}^{+} & 0 & 0\\
\exp(iDK_{z1}) & \exp(iDK_{z2}) & \exp(iDK_{z3}) & \exp(iDK_{z4}) & 0 & 0 & -\exp(iDk_z) & 0\\
\exp(iDK_{z1})\overline{K}_{z1} & \exp(iDK_{z2})\overline{K}_{z2} & \exp(iDK_{z3})\overline{K}_{z3} & \exp(iDK_{z4})\overline{K}_{z4} & 0 & 0 & -\exp(iDk_z)\overline{k}_z & 0\\
\exp(iDK_{z1})\overline{K}_{z1}^2 & \exp(iDK_{z2})\overline{K}_{z2}^2 & \exp(iDK_{z3})\overline{K}_{z3}^2 & \exp(iDK_{z4})\overline{K}_{z4}^2 & 0 & 0 & -\exp(iDk_z)\overline{\kappa}_z^2 & \exp(iDh^{-})v_{-H}\\
\exp(iDK_{z1})\overline{K}_{z1}^3 & \exp(iDK_{z2})\overline{K}_{z2}^3 & \exp(iDK_{z3})\overline{K}_{z3}^3 & \exp(iDK_{z4})\overline{K}_{z4}^3 & 0 & 0 & -\exp(iDk_z)\overline{k}_z\overline{\kappa}_z^2 & -\exp(iDh^{-})v_{-H}\overline{h}^{-}
\end{pmatrix}
\times\begin{pmatrix}u_1\\u_2\\u_3\\u_4\\s\\b\\t\\l\end{pmatrix}=\begin{pmatrix}1\\\overline{k}_z\\\overline{\kappa}_z^2\\\overline{k}_z\overline{\kappa}_z^2\\0\\0\\0\\0\end{pmatrix}. \tag{112}$$

The many vanishing matrix elements allow us to easily eliminate s, b, t, l leaving four equations for u_n:

$$\begin{pmatrix} \overline{k}_1^+ & \overline{k}_2^+ & \overline{k}_3^+ & \overline{k}_4^+ \\ -\overline{h}_1^+\overline{\kappa}_1^2 & -\overline{h}_2^+\overline{\kappa}_2^2 & -\overline{h}_3^+\overline{\kappa}_3^2 & -\overline{h}_4^+\overline{\kappa}_4^2 \\ \exp(iDK_{z1})\overline{k}_1^- & \exp(iDK_{z2})\overline{k}_2^- & \exp(iDK_{z3})\overline{k}_3^- & \exp(iDK_{z4})\overline{k}_4^- \\ \exp(iDK_{z1})\overline{h}_1^-\overline{\kappa}_1^2 & \exp(iDK_{z2})\overline{h}_2^-\overline{\kappa}_2^2 & \exp(iDK_{z3})\overline{h}_3^-\overline{\kappa}_3^2 & \exp(iDK_{z4})\overline{h}_4^-\overline{\kappa}_4^2 \end{pmatrix} \begin{pmatrix} u_1 \\ u_2 \\ u_3 \\ u_4 \end{pmatrix} = \begin{pmatrix} 2\overline{k}_z \\ 0 \\ 0 \\ 0 \end{pmatrix}. \tag{113}$$

The solution is

$$\begin{pmatrix} u_1 \\ u_2 \\ u_3 \\ u_4 \end{pmatrix} = \frac{2\overline{k}_z}{N} \begin{pmatrix} 0 & g_{34} & g_{42} & g_{23} \\ g_{43} & 0 & g_{14} & g_{31} \\ g_{24} & g_{41} & 0 & g_{12} \\ g_{32} & g_{13} & g_{21} & 0 \end{pmatrix} \begin{pmatrix} \overline{h}_1^+\overline{\kappa}_1^2 \\ \overline{h}_2^+\overline{\kappa}_2^2 \\ \overline{h}_3^+\overline{\kappa}_3^2 \\ \overline{h}_4^+\overline{\kappa}_4^2 \end{pmatrix}, \tag{114}$$

$$g_{\alpha\beta} = \exp[iD(K_{z\alpha} + K_{z\beta})]\left(\overline{h}_\alpha^-\overline{\kappa}_\alpha^2\overline{k}_\beta^- - \overline{h}_\beta^-\overline{\kappa}_\beta^2\overline{k}_\alpha^-\right), \tag{115}$$

$$N = \sum_{(\alpha\beta\gamma\delta)} g_{\alpha\beta}\left(\overline{h}_\delta^+\overline{\kappa}_\delta^2\overline{k}_\gamma^+ - \overline{h}_\gamma^+\overline{\kappa}_\gamma^2\overline{k}_\delta^+\right), \tag{116}$$

$$(\alpha, \beta, \gamma, \delta) \in \{(1,2,3,4),(1,3,4,2),(1,4,2,3),(2,3,1,4),(2,4,3,1),(3,4,1,2)\}. \tag{117}$$

Using lines 1, 3, 5 and 7 in equation (112) we determine s, b, t, l from u_n:

$$s = -1 + \sum_{n=1}^{4} u_n, \qquad b = \frac{1}{v_{-H}} \sum_{n=1}^{4} \overline{\kappa}_n^2 u_n, \tag{118}$$

$$t = \sum_{n=1}^{4} \exp(-iDk_n^-)u_n, \qquad l = \frac{1}{v_{-H}} \sum_{n=1}^{4} \overline{\kappa}_n^2 \exp(iDh_n^-)u_n. \tag{119}$$

We insert u_n [equation (114)] and simplify the result using Vieta's formulas [equations (94)–(99)] and the original quartic equation (5).

$$s = \frac{1}{N} \sum_{(\alpha\beta\gamma\delta)} g_{\alpha\beta}\left(\overline{h}_\delta^+\overline{\kappa}_\delta^2\overline{k}_\gamma^- - \overline{h}_\gamma^+\overline{\kappa}_\gamma^2\overline{k}_\delta^-\right), \tag{120}$$

$$b = \frac{2\overline{k}_z}{Nv_{-H}} \sum_{(\alpha\beta\gamma\delta)} g_{\alpha\beta}(\overline{K}_{z\delta} - \overline{K}_{z\gamma})\overline{\kappa}_\gamma^2\overline{\kappa}_\delta^2, \tag{121}$$

$$t = \frac{-2\overline{k}_z}{N} \exp[-iD(2H_z + k_z)] \sum_{n=1}^{4} \exp(-iDK_{zn}) B_n (\overline{h}_n^+)^2 \overline{\kappa}_n^2, \tag{122}$$

$$l = \frac{2\overline{k}_z v_H}{N} \exp[-iD(H_z + k_{Lz})] \sum_{n=1}^{4} \exp(-iDK_{zn}) B_n \overline{h}_n^+ \overline{k}_n^+, \tag{123}$$

$$B_1 = (\overline{K}_{z2} - \overline{K}_{z3})(\overline{K}_{z3} - \overline{K}_{z4})(\overline{K}_{z4} - \overline{K}_{z2}), \tag{124}$$

$$B_2 = (\overline{K}_{z1} - \overline{K}_{z4})(\overline{K}_{z4} - \overline{K}_{z3})(\overline{K}_{z3} - \overline{K}_{z1}), \tag{125}$$

$$B_3 = (\overline{K}_{z1} - \overline{K}_{z2})(\overline{K}_{z2} - \overline{K}_{z4})(\overline{K}_{z4} - \overline{K}_{z1}), \tag{126}$$

$$B_4 = (\overline{K}_{z1} - \overline{K}_{z3})(\overline{K}_{z3} - \overline{K}_{z2})(\overline{K}_{z2} - \overline{K}_{z1}). \tag{127}$$

As a first quality test of the results we check whether the neutron flux is conserved. We have set the amplitude of the incident plane wave to unity, so the intensity entering through a surface unit area is given by $I_0 = 1/\cos\gamma$ with the incident angle γ (*cf.* Fig. 12). The transmitted and the surface reflected components are exiting under the same angle with the intensities $I_S = |s|^2/\cos\gamma$ and $I_T = |t|^2/\cos\gamma$, respectively. The two diffracted components exit under γ_L with the intensities $I_B = |b|^2/\cos\gamma_L$ and $I_L = |l|^2/\cos\gamma_L$, respectively. The relation of flux conservation reads $I_S + I_B + I_T + I_L = I_0$ or

$$\frac{|s|^2}{\cos\gamma} + \frac{|b|^2}{\cos\gamma_L} + \frac{|t|^2}{\cos\gamma} + \frac{|l|^2}{\cos\gamma_L} = \frac{1}{\cos\gamma}. \tag{128}$$

The computed result is $I_S + I_B + I_T + I_L - I_0 \lesssim 10^{-4} I_0$ and with numerically polished $\overline{K}_z$ values $\lesssim 2 \times 10^{-8} I_0$. Only close to the transition between the Bragg and Laue cases, *i.e.* at grazing exit angles, do the formulas seem to be numerically unstable, as the conservation of intensity is violated by 10%. The instability is probably related to the infinite slope of $\overline{K}_{z2,3}$ in Fig. 14(*b*) at the Bragg/Laue boundary and could be solved only by a parameterization other than $\overline{K}_z$ in the original equation (79).

The exponential terms in equation (115) can diverge numerically if the values of $\overline{K}_z$ become complex. To avoid numerical errors we created a C++ class consisting of three long double values a, b, x such that each complex number can be represented by $(a + ib)\exp(x)$. The exponential term is

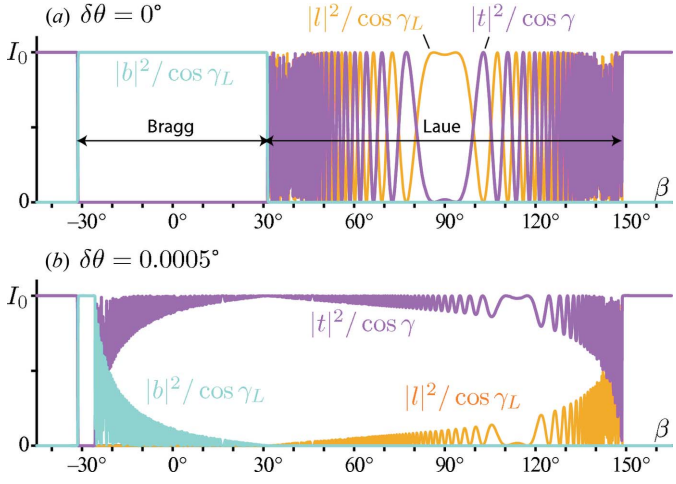

Figure 15
Transmitted (t) and diffracted (b, l) intensities *versus* Bragg-plane orientation β, calculated for a 1 mm thick silicon sample and 220 Bragg planes. The surface reflected intensity is in the order of 10^{-6} and not visible in the plot. In (*a*) the Bragg condition is exactly fulfilled. In the Bragg range the intensity is totally reflected, while in the Laue range the typical *Pendellösung* oscillations between transmitted and diffracted beam are visible. In (*b*) the incident angle is off-Bragg by 0.0005° or about three Darwin widths. For $\beta \lesssim -32°$ and $\beta \gtrsim 150°$ no diffraction occurs because the reciprocal-lattice vector **H** as defined by equation (58) points into the wrong direction.

preserved as long as arithmetic operations allow it. This way the exponential terms in the denominator and numerator of s, b, t, l finally cancel.

Fig. 15 shows the calculated intensities for a silicon sample.

Another test is the comparison with the formulas in equations (19), (20) and (29), (30) of the symmetric cases. The agreement for the silicon sample is $|\mathrm{abs}(t) - \mathrm{abs}(t_{\mathrm{sym}})| \lesssim 10^{-6}|t|$ and $|\arg(t) - \arg(t_{\mathrm{sym}})| \lesssim 10^{-7}2\pi$. A better agreement cannot be expected since the symmetric formulas do not take surface reflection into account.

Fruitful discussions with Claudio Ferrero, Jean-Pierre Guigay, Erwin Jericha and Helmut Rauch are gratefully acknowledged.

References

Authier, A. (1998). *Cryst. Res. Technol.* **33**, 517–533.
Authier, A. (2006). *Dynamical Theory of X-ray Diffraction*. Oxford University Press.
Batterman, B. W. & Cole, H. (1964). *Rev. Mod. Phys.* **36**, 681–717.
Bauspiess, W., Bonse, U. & Graeff, W. (1976). *J. Appl. Cryst.* **9**, 68–80.
Bonse, U. & Graeff, W. (1977). *X-ray Optics*, Vol. 22 of *Topics in Applied Physics*, *X-ray and Neutron Interferometry*. Heidelberg: Springer Verlag.
Dickson, L. E. (1914). *Elementary Theory of Equations*, pp. 38–46. New York: John Wiley & Sons, Inc.
Ioffe, A., Jacobson, D. L., Arif, M., Vrana, M., Werner, S. A., Fischer, P., Greene, G. L. & Mezei, F. (1998). *Phys. Rev. A*, **58**, 1475–1479.
Lemmel, H. (2007). *Phys. Rev. B*, **76**, 144305.
Lemmel, H. & Wagh, A. G. (2010). *Phys. Rev. A*, **82**, 033626.
Petrascheck, D. (1976). *Acta Phys. Austriaca*, **45**, 217–231.
Petrascheck, D. (1987). *Phys. Rev. B*, **35**, 6549–6553.
Press, W. H., Teukolsky, S. A., Vetterling, W. T. & Flannery, B. P. (2002). *Numerical Recipes in C++*. Cambridge University Press.
Rauch, H. & Werner, S. A. (2000). *Neutron Interferometry*. Oxford: Clarendon Press.
Sears, V. F. (1982). *Phys. Rep.* **81**, 1–29.
Sears, V. F. (1985). *Z. Phys. A*, **321**, 443–449.
Springer, J. (2009). PhD thesis, Vienna University of Technology, Austria.
Springer, J., Zawisky, M., Lemmel, H. & Suda, M. (2010). *Acta Cryst.* A**66**, 17–21.
Vrána, M., Mikula, P., Lukáš, P., Ioffe, A. & Nistler, W. (2000). *Physica B*, **283**, 400–402.